

**Simulations for the
Measurement of the Polarizabilities
of the Pion at COMPASS**

**Diploma Thesis
by
Roland Kuhn**

**Technische Universität München
Physik-Department E18
November 2001**

Abstract

A Monte Carlo simulation of the process $\pi^- N \rightarrow \pi^- \gamma N$ is performed to study the feasibility of the measurement of the pion polarizabilities $\bar{\alpha}$ and $\bar{\beta}$ with the COMPASS spectrometer at CERN. The detector setup is examined to locate the sources of loss in acceptance and efficiency and to investigate systematic errors. Five data samples à 620.000 events—each corresponding to half a day of COMPASS data taking—are generated and analyzed to study event selection algorithms and reconstruction. The statistical error achievable by one month of COMPASS data taking is estimated to $0.02 \cdot 10^{-4} \text{ fm}^3$ for $\bar{\alpha} + \bar{\beta}$ and $0.14 \cdot 10^{-4} \text{ fm}^3$ for $\bar{\alpha} - \bar{\beta}$. The strength of the hadronic background is investigated by means of $4.5 \cdot 10^6$ minimum bias events generated with Fritiof. The suppression factor for this background—only taking into account the effect of kinematic cuts—is estimated to $6 \cdot 10^{-6}$, resulting in a signal to noise ratio of 50.

Contents

1	Introduction	1
2	The COMPASS Experiment	3
2.1	COMPASS physics	3
2.1.1	Experiments with the muon beam	4
2.1.2	Experiments with the hadron beam	5
2.2	The experimental setup	6
2.2.1	Design overview	7
2.2.2	The magnets	7
2.2.3	Detector types	8
2.2.4	The target region	11
2.2.5	Tracking downstream of SM1	12
2.2.6	Identification	12
3	Primakoff Scattering	15
3.1	Polarizabilities of hadrons	15
3.2	The kinematics	16
3.2.1	In the laboratory frame	16
3.2.2	In the projectile frame	21
3.2.3	Mandelstam variables	23
3.3	The Weizsäcker-Williams approximation	23
3.3.1	Semi-classical	23
3.3.2	Covariant	24
3.4	Low energy theorems in QED	25
3.5	The Primakoff mechanism	27
3.6	Combining the ingredients	27
3.7	Predictions and Measurements	28

CONTENTS

4	The Monte Carlo Setup	31
4.1	The general idea	31
4.2	The event generators	33
4.2.1	Single particle generator	33
4.2.2	Polaris	33
4.2.3	Fritiof	34
4.3	Particle tracking	34
4.4	COMPASS reconstruction software	36
4.5	The analysis software	37
4.6	Testing the prerequisites	38
4.6.1	Tests with single π^- events	39
4.6.2	Tests with single γ events	47
4.6.3	Test summary	52
5	Simulation	53
5.1	The run conditions	53
5.2	The reconstruction method	54
5.3	Rate estimates	57
5.4	Retrieving the polarizabilities	58
5.5	Strength of hadronic background	62
5.6	Influence of systematic reconstruction errors	65
6	Conclusion and Outlook	67
Appendix		
A	Design of the computing cluster	69
A.1	The hardware	69
A.2	The software	69
A.3	Performance	70
B	Single particle generator	71
C	The detector setup	75
Bibliography		83

List of Figures

The COMPASS experiment

2.1 Schematic of the COMPASS detector	6
---	---

Primakoff scattering

3.1 Momentum conservation for longitudinal momentum transfer . . .	18
3.2 Photon momentum for longitudinal momentum transfer	18
3.3 Momentum conservation in the general case	19
3.4 Photon energy and angle in the projectile frame	22
3.5 Weizsäcker-Williams photon energy spectrum	24
3.6 Compton scattering feynman graphs	25
3.7 Differential cross section in the projectile frame	28

Tests with π^- , all interactions disabled

4.1 Generated momentum distribution	40
4.2 Generated θ distribution	40
4.3 x and y momentum components	40
4.4 Relative momentum reconstruction error	40
4.5 Angular resolution vs. P	41

Tests with π^- , all interactions enabled

4.6 Relative momentum reconstruction error	43
4.7 Reconstruction efficiency	43
4.8 Angular resolution vs. P	43
4.9 Momentum reconstruction error for bad events	44
4.10 Momentum reconstruction error for bad events	45
4.11 Momentum reconstruction error	45
4.12 Direction reconstruction error	45
4.13 Reconstruction efficiency	46
4.14 Angular resolution with fit parameters	46

Tests with γ

4.15 Energy and direction	48
-------------------------------------	----

LIST OF FIGURES

4.16	<i>z</i> -coordinate of conversion vertex	48
4.17	Reconstruction efficiency	48
4.18	Direction reconstruction error	48
4.19	Photon energy and direction for bad events	49
4.20	Energy resolution	50
4.21	Relative position of HCAL hit	51
4.22	Energy in HCAL	51
4.23	Energy resolution after leakage correction	51
Simulation		
5.1	Photon energy in the laboratory frame	54
5.2	Reconstruction efficiency for Primakoff	54
5.3	Reconstructed beam energy	55
5.4	Four-momentum transfer: q^2	55
5.5	q_E	55
5.6	q_z	55
5.7	q_x	55
5.8	q_y	55
5.9	Generated count rates with fit parameters	59
5.10	Reconstructed cross section with fit parameters	59
5.11	Correlation plot between $\bar{\alpha}$ and $\bar{\beta}$	60
5.12	Correlation plot between flux factor and $\bar{\alpha}$	60
5.13	Generated and reconstructed polarizabilities	61
5.14	Distribution of accepted background	62
5.15	Reconstructed beam energy for background events	62
Appendix		
	Detailed schematic of COMgeant geometry setup	76

Chapter 1

Introduction

The pion plays a major role in tying together the protons and neutrons to form nuclei. It is therefore desirable to gain a better understanding of the properties of this particle. While charge and quark content of the pion are well established little is known about its internal structure. What happens if it is exposed to an intense electric or magnetic field? The response of the pion to this environment is characterized by its electric and magnetic polarizability.

Unfortunately the pion only survives for a very short time, so these parameters cannot be measured with pions at rest. The COMPASS experiment with its pion beam, high resolution spectrometer and high rate data acquisition is well-suited for a measurement of these parameters. The intense electromagnetic field to test the response is provided by a Lead target: the internal electric field of these atoms is 1000 times higher than the one that produces atmospheric lightning.

In order to prepare such a measurement the spectrometer has to be built and tested, but it is also necessary to become familiar with the properties of the apparatus. Without the possibility to access the hardware the preferred procedure is to make a Monte Carlo simulation.

The name Monte Carlo recalls the vision of a casino. At such a place bets are made about events that are purely random. Ideally nobody knows in advance what the outcome will be. The application of the term in science has a twofold connection to this meaning: the problems that are analyzed using this technique usually are so complex that it is not possible to tell the exact outcome beforehand and the method itself depends on the randomness of some of the individual steps that are done during such a simulation.

An example: the movement of atoms in a gas is described by the scattering of the atoms on each other. Even if the mechanism of the scattering process is completely known it is not possible to calculate how probable it is to find a specific

1 INTRODUCTION

atom at a given time in a given volume of the gas because of the great number of variables that have influence on the result. The question can be answered approximately by choosing the starting configuration and simulating several scattering processes. Because of quantum mechanics the exact result of the scattering is not determined. There are only probabilities for each possible outcome, so one of those is chosen in a—ideally—non-deterministic manner by the simulation. After a number of steps the position of the atom is drawn on the screen and the simulation starts again with the same starting conditions as before.

While each single simulation only produces a special solution of the problem the picture evolving on the screen contains more information: the density of points corresponds to the probability to find the atom in a given region. The mathematically exact but inaccessible solution is approximated by a method that scales with the computing power at hand and is, apart from that, only limited by the precision of the description of the problem.

The COMPASS spectrometer is a very complex apparatus. The motion of the particles that is to be detected is influenced by the detectors, and the limitations on a successful reconstruction of their paths depend on their initial parameters in a way that is not simple to describe. While in the experimental hall the physical effects cannot be switched off to sort out different influences this is possible in a simulation. Also the simulation permits better insight in the processes that happen. The main motivation is to use this controlled environment to learn details about the apparatus that are experimentally inaccessible.

Chapter 2

The COMPASS Experiment

COMPASS stands for **C**ommon **M**uon and **P**roton **A**pparatus for **S**tructure and **S**pectroscopy. Being a merger of the HMC¹ and CHEOPS² projects, COMPASS will examine a variety of effects in high energy physics. It is a fixed target experiment supplied with the 400 GeV proton beam of the CERN³ SPS⁴. The beam line is capable of transporting either these protons or a secondary beam gained by inserting a production target. Depending on the polarity of the bending magnets the secondary particles either are a mixture of p^+ , π^+ , K^+ or π^- , K^- . The yield of these particles is high enough to select secondary beam energies up to 270 GeV.

Since the distance from the production target to the experiment is about 1 km a muon beam also is available: the π^- decays into a μ^- and an antineutrino. Because of the time dilatation the mean life of the pion beam is about 8 km so the intensity of the muon beam is much lower than that of the hadron beam at the same energy; as a compromise 160 GeV are chosen. To purify the muon beam a heavy concrete absorber is placed in front of the experiment stopping hadron content while causing only a small energy loss to the muons.

2.1 COMPASS physics

Further details concerning the physics program mentioned below can be found in [CO96].

¹Hadron Muon Collaboration, [HMC95]

²Charm Experiment with OmniPurpose Setup, [CHE95]

³European Laboratory for Nuclear Research, Geneva, Switzerland

⁴Super Proton Synchrotron

2.1.1 Experiments with the muon beam

2.1.1.1 Gluon polarization

Since the measurements of EMC [EMC88] it is clear that the spin of the nucleon cannot be constructed only of the spins of the quark content. Other sources are angular momentum of the quark or gluon content or gluon polarization, the latter being the most prominent explanation.

To test this hypothesis a direct measurement of the gluon helicity distribution $\Delta G(x)$ will be performed by means of the longitudinal spin asymmetry of open charm leptoproduction [GR88]. This measurement is based on the reconstruction of D^0 mesons from their hadronic decay products and requires a polarized target and beam.

2.1.1.2 Lambda polarization

Complementary information about the spin structure of the nucleon can be gained by examining the polarization of the strange sea⁵. This is done via semi-inclusive deep inelastic scattering of longitudinally polarized muons on unpolarized and longitudinally polarized nucleons producing polarized lambda hyperons in the current fragmentation region (cf. [CO96] and references therein).

2.1.1.3 Longitudinal spin distribution functions

To further investigate the various models for the spin structure of the nucleon a measurement of the polarized parton distribution functions is needed. This can be achieved by semi-inclusive measurements of deep inelastic scattering of polarized leptons on polarized proton and deuteron targets [EMC89]. The produced π^+ , π^- , K^+ and K^- mesons are identified by a RICH⁶. From the asymmetries in the production rates for different polarizations the spin distribution functions of the valence and of the non-strange sea quarks can be calculated.

2.1.1.4 Transverse spin distribution functions

As shown by Jaffe and Ji [JJ91, JJ92] the quark state inside the nucleon at the twist-two level is completely specified by the momentum distributions $q(x)$, the

⁵Since the nucleon consists only of u and d valence quarks the heavier flavors like s and c only are present as vacuum fluctuations. These fluctuations of $q\bar{q}$ pairs are called sea quarks.

⁶Ring Imaging Cherenkov detector

helicity distributions $\Delta q(x)$ and the transverse spin distributions $\Delta_{\tau}q(x)$. Since the latter have not yet been measured this will be done using the Collins effect for leading pions [Col93]. This effect produces an azimuthal dependence of the fragmentation function for transversely polarized quarks.

2.1.2 Experiments with the hadron beam

2.1.2.1 Charmed hadrons

While charmed mesons are the object of intense studies, little is known about the properties of charmed baryons. For example of the $J^P \frac{3}{2}^+$ 20-plet the Σ_c^{0*} and Ω_c^{0*} are still unconfirmed. In analogy to the $D^{*+} \rightarrow D^0\pi^+$ tagging mechanism transitions like $\Omega_c^{0*} \rightarrow \Omega_c^0\pi^0$ can be used.

Even more interesting is the still untackled issue of double-charmed baryons. These lie within the 3.5–4 GeV mass region and are challenging as they are hard to produce and difficult to identify.

2.1.2.2 Gluonic systems

An unconfirmed prediction of QCD⁷ is the existence of non- $q\bar{q}$ mesons consisting only [FG72] or in part [Z⁺86] of glue. These glue balls or hybrids are hard to identify because they are expected in the 1.5–2 GeV mass region. In this region many meson resonances are seen which will mix with objects of identical quantum numbers. Since the predicted width of such an object is 100–150 MeV it should be possible to disentangle it from neighboring resonances by high statistics studies of all contributing states.

2.1.2.3 Hadronic structure

In addition to the measurement of the polarizabilities of the pion, kaon and sigma beams will permit similar measurements on these particles. In contrast to the situation for the pion there is currently no data available in this context.

Another field of interest is the chiral anomaly. It is described by an additional term in the chiral Lagrangian and makes possible parity violating transitions between an even and odd number of mesons in the initial and final states. Better experimental data is needed to test e. g. $\mathcal{O}(p^6)$ corrections as computed in [B⁺90] to the process $\gamma \rightarrow 3\pi$.

⁷Quantumchromodynamics

2 THE COMPASS EXPERIMENT

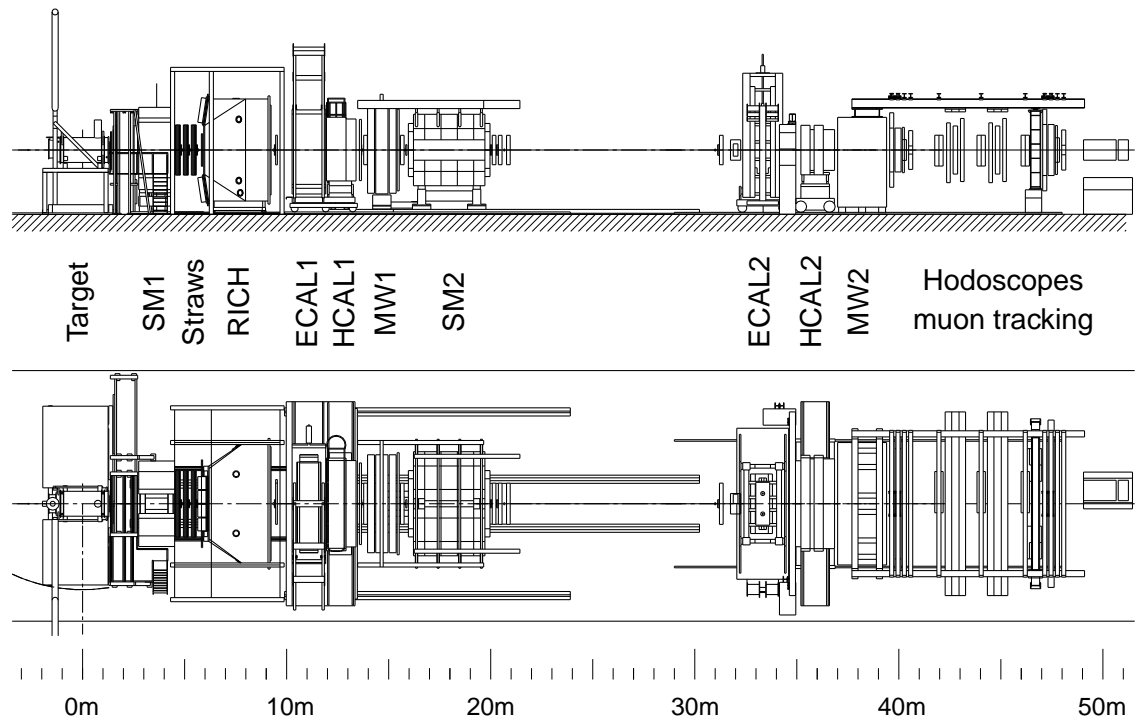


Figure 2.1: Side and top view of the COMPASS spectrometer with the polarized target for the muon program

2.1.2.4 Exotics

Several objects like the singly charmed Pentaquark $uud\bar{c}s$ [GSR87] or the doubly charmed Tetraquark $cc\bar{u}\bar{d}$ [Ric91] are expected to be seen. In general many color neutral objects are expected to exist, e. g. mesons of the type $q\bar{q} q\bar{q}$ or $qq \bar{q}\bar{q}$, but it is not clear which constellations are bound states.

2.2 The experimental setup

This section does not describe the detector as it can be visited now in the hall but the setup that was used for the simulation. It is the official hadron setup, enriched with the number of silicon trackers and GEMs projected for 2002. Thus, it is not guaranteed to match the configuration that will actually be used for the measurement.

Compared to the proposal [CO96] much has changed. The biggest modifications concern the first spectrometer magnet and the type of tracking detectors where honeycomb trackers were replaced by gas electron multipliers.

2.2.1 Design overview

In order to achieve a good energy resolution within a wide energy range COMPASS is designed as a two stage spectrometer with a 1.0 Tm and a 5.2 Tm conventional magnet. The tracking stations are composed of different detector types to cover a large area while achieving a good spatial resolution in the vicinity of the beam. Most of the tracking detectors operate on the principle of gas amplification, for a review see [Sau77].

In the first stage a ring imaging cherenkov detector is used to distinguish pions, kaons and protons. At the end of each stage an electromagnetic and a hadronic calorimeter detects the energies of the incident photons, electrons and hadrons. After the calorimeters a muon wall filters out all shower remnants and detects the position of the passing muons. The calorimeters and muon wall of the first stage have a hole of $1.4 \times 0.7 \text{ m}^2$ to let pass the particles with higher energy to the second stage.

The trigger can be composed of a beam veto, a target recoil detector, the calorimeters and various hodoscopes. The target platform is moveable to make possible the exchange of the polarized target by a normal solid state target, e. g. a cylindrical lead plate 40 mm in diameter and 3 mm in width.

2.2.2 The magnets

A magnetic spectrometer makes use of the Lorentz force to determine the ratio of charge to momentum of a particle. If ℓ is the extent of the field of strength B , q the charge of a particle with momentum $p = \beta\gamma mc$, then the radius r of the circular trajectory of the particle inside the field is

$$\frac{\gamma m \beta^2 c^2}{r} = q \beta c B \quad \Rightarrow \quad r = \frac{p}{qB} \quad (2.1)$$

For small angles the deflection $\phi \approx \frac{\ell}{r}$ is anti-proportional to the momentum:

$$\phi = \frac{q\ell B}{p} \quad (2.2)$$

Thus, the higher the particle's momentum, the smaller is its deflection in the magnetic field, so a better spatial resolution is needed for small angles to retain a certain momentum resolution.

2 THE COMPASS EXPERIMENT

2.2.2.1 SM1

The first spectrometer magnet is located 3.63 m downstream of the target. It is a conventional magnet with a bending power⁸ of 1.0 Tm and has a gap of 172 cm that is opening downstream. This design provides a bigger acceptance and yields a better momentum resolution for particles with a big angle to the beam but also raises the problem of forces between the magnet and its surroundings.

Since Primakoff scattering occurs under very small angles a more concentrated field would be desirable. This could be achieved by lowering the gap to 120 cm. As a side effect the issues of substantial fringe fields would nearly vanish. It is not yet clear if this can be changed in a reasonable amount of time, so this simulation was done with the wider gap.

2.2.2.2 SM2

The second spectrometer magnet is also a conventional magnet located 17.83 m downstream of the target. It can be operated with currents of 2000 A to 5000 A. The maximum current—providing a bending power of 5.2 Tm—was used in this simulation. The gap of SM2 is $4 \times 2 \times 1 \text{ m}^3$ ($d \times w \times h$).

2.2.3 Detector types

2.2.3.1 Scintillating fibers

Using fast scintillation in plastic fibers, this detector has a time resolution of about 0.3 ns [Teu01]. Each station consists of two or three multilayers of fibers, giving the projections 0 deg/90 deg or 0 deg/45 deg/90 deg. These detectors are crucial for the track timing and therefore are optimized for speed while the spatial resolution is 500 μm .

2.2.3.2 Silicon microstrips

For a review on silicon microstrip detectors see [Pei92]. One station of silicon microstrips consists of two $5 \times 7 \text{ cm}^2$ silicon wafers with two-dimensional readout mounted 1 cm apart. To be able to separate multiple hits the strips on one wafer are rotated 5 deg with respect to the strips on the other.

The spatial resolution is 7 μm and the time resolution is better than 5 ns [Fri01].

⁸The integrated field strength, $\int B d\ell$.

2.2.3.3 Micromegas

This detector is similar in size and function to the GEMs described below, using one copper mesh instead of three copper plated foils (cf. [T⁺01]). This makes the Micromegas design more robust to sparks which occur frequently within this detector. As for the GEM one station consists of two Micromegas chambers mounted back to back having one rotated by 45 deg.

The spatial resolution is about 70 μm while the time resolution is better than 10 ns.

2.2.3.4 Drift chambers

There is one station of drift chambers installed right after SM1. The active area is $140 \times 124 \text{ cm}^2$ with a cylindric passivated area of 30 cm diameter. Each of the projections 0 deg, 90 deg, 20 deg and -20 deg is equipped with two readout planes. The wires of corresponding planes are displaced by 3.5 mm with respect to each other and have a pitch of 7 mm. The distance between planes is 8 mm.

This detector is read with TDCs and has a spatial resolution of 175 μm per projection [SDC]. Since it uses the drift time in the spatial measurement it does not give timing information apart from the 70 ns time window that is given by the maximum drift time of the charge cloud.

2.2.3.5 Gas electron multipliers

Gas Electron Multiplier [Sau97] will be abbreviated GEM. It consists of three amplification foils $30 \times 30 \text{ cm}^2$ in size which are copper plated on both sides and perforated with 70 μm holes in an hexagonal pattern with a pitch of 120 μm . By applying a voltage of about 380 V across each foil and corresponding voltages between them an amplification factor of 6000 can be achieved. Below the bottom foil is placed a PCB for two-dimensional readout. The central region of the amplification foils can be deactivated to protect them from the radiation of the beam. The resulting passivated area is 5 cm in diameter and will be covered with a silicon station in most cases. Each GEM station consists of two GEMs mounted back to back on one frame, one of them rotated by 45 deg.

The spatial resolution is $46 \pm 3 \mu\text{m}$ [Sim01], the time resolution is about 15 ns.

2.2.3.6 Straw chambers

For large angle tracking after SM1 very big detectors are needed. These are made of aluminum coated kapton tubes with an anode wire in the center and a shielding of carbon coated mylar (cf. [SW99]). There are two types of tubes being 10 mm and 6 mm in diameter. These tubes are mounted in double layers to get full spatial acceptance. The active area is divided parallel to the wires in three parts, the inner third using the 6 mm tubes to improve the resolution in the vicinity of the $20 \times 20 \text{ cm}^2$ beam hole.

The active area of one double layer is $273 \times 325 \text{ cm}^2$ either with horizontal or vertical wires. The latter are also available tilted by $\pm 10 \text{ deg}$ giving in total the same four projections as for the MWPCs. From the readout point of view these detectors are very similar to the drift chambers. The spatial resolution of one double layer is $150 \mu\text{m}$.

2.2.3.7 Multiwire proportional counters

The well established technology of MWPCs (see e.g. [Sau77] for a review) is widely used in COMPASS. The chambers were refurbished from the OMEGA spectrometer of the WA89 experiment at CERN. These detectors have a wire pitch of 2 mm resulting in a spatial resolution of 0.5 mm. Wires can be mounted in the projections 0 deg, 10 deg, -10 deg and 90 deg and cover an active area of $150 \times 120 \text{ cm}^2$. The station after SM1 has all four projections, stations before the second muon wall have all but 90 deg and the stations after the second muon wall are equipped alternating with 10 deg/0 deg and -10 deg/0 deg. All MWPCs have a passivated area for the beam sizing from 16 cm in diameter to 22 cm in diameter depending on the distance from the target.

2.2.3.8 Electromagnetic calorimeter

The electromagnetic calorimeter has to fulfill equally high requirements in spatial and energy resolution. COMPASS therefore takes advantage of the GAMS calorimeter⁹ half of which is reused as ECAL2 in the second spectrometer. This calorimeter is made up of 2044 lead glass crystals sized $4 \times 4 \times 45 \text{ cm}^3$. It has an active area of $128 \times 256 \text{ cm}^2$ and a beam hole of $8 \times 8 \text{ cm}^2$.

According to the specification the parameters of this detector are (energy E measured in units of GeV):

⁹see [B⁺85] for details

- energy resolution: $\frac{\sigma_E}{E} = \frac{0.055}{\sqrt{E}} \oplus 0.015$
- position resolution: $\sigma_x = \frac{6 \text{ mm}}{\sqrt{E}} \oplus 0.5 \text{ mm}$
- minimum photon energy: 20 MeV

2.2.3.9 Hadronic calorimeter

The main task of the first hadronic calorimeter HCAL1 is the detection of neutrons from charmed baryon decays. Due to the low energy of these neutrons position resolution is more important than energy resolution. The calorimeter consists of $15 \times 15 \times 100 \text{ cm}^3$ cells arranged in a 28×20 matrix which has a hole of 8×4 cells in the center. The energy resolution is $\sigma_E/E = 0.8/\sqrt{E} \oplus 0.08$ with a spatial resolution ranging from 4 mm to 14 mm depending on the position of the hit inside one cell.

More important for Primakoff events is the second hadronic calorimeter HCAL2. It is optimized for energy resolution wherefore the sandwich structure of the cells is 16 mm lead and 4 mm scintillator. The $20 \times 20 \times 120 \text{ cm}^3$ cells are arrayed in a 22×10 matrix resulting in an active area of $4.4 \times 2 \text{ m}^2$. The energy resolution is $\sigma_E/E = 0.6/\sqrt{E} \oplus 0.06$.

2.2.4 The target region

The target region has a special setup that is changed according to the requirements of the intended measurement. A polarized Deuterium target is used for measuring spin dependent observables like $\frac{\Delta G}{G}$ with a muon beam. It consists of a superconducting magnet with two cylindric chambers for anti-parallel polarized target cells positioned along the beam axis. Because of the size of the target solenoid there is no space for small angle trackers between the interaction point and SM1, so there are only two stations of silicon microstrips and two stations of scintillating fibers tracking the beam particle before entering the target.

In the hadron setup the rather huge target cryostat is replaced by a simple solid state target with a recoil detector. This leaves space for two silicon trackers between the target and SM1. These are essential for Primakoff reactions as the scattering angle has to be measured with a precision better than 1 mrad because it contains much of the information. The silicon microstrip detectors offer an excellent spatial resolution while being able to withstand high particle rates.

The recoil detector is currently developed and tested. According to [Olc01] a particle momentum of about 100 MeV should be sufficient to trigger a veto coincidence in its scintillator and Lead glass layers. This veto will limit the angular acceptance to about 100 mrad to reject events where fragments of the nucleus or particles produced in diffractive processes leave the target with bigger angles to the beam axis.

2.2.5 Tracking downstream of SM1

The higher a particle's energy the smaller is its deflection in the magnetic field; thus high energy particles will have a very small angle between their direction of flight and the beam direction. This demands higher spatial resolution of the tracking stations in the vicinity of the beam to be able to detect such high energy particles.

In general, the tracking stations are composed of a large area tracker like a straw chamber or an MWPC, a GEM or Micromegas station and finally a silicon or scintillating fiber station. As most of the beam particles hardly interact with the target the center of each tracking station is hit at very high rate and density. Silicon detectors were chosen for this region because the created electron-hole pairs are drained off the depletion zone in less than 100 ns while detectors using gas amplification have much larger regeneration times. Also the spatial resolution is best for the given detector types which permits the finding of tracks with very low inclination to the beam.

For track finding the detector is divided into four zones: before the first magnet, between the magnets, between the second magnet and the second muon wall and after the second muon wall. Inside one zone tracks are assumed to be straight lines. Thus finding a track is done by first finding all straight lines between hits in one zone, bridging these candidates through the magnetic fields and finally fitting the resulting tracks and vertices to the actual hit positions.

The pattern recognition begins to work efficiently when at least three planes per projection are available inside each zone. Detector planes which do not have enough neighbors can still be used in later steps to resolve ambiguities and improve overall precision.

2.2.6 Identification

There are different identification mechanisms for the long living particles. Muons are the only ones to be seen after the muon filters. Electrons produce a track

which is heading towards a corresponding hit in the calorimeter. Photons are only seen in the calorimeter, but there is a rather high probability for them to convert into an e^+e^- -pair which has to be reconstructed. Neutral pions decay rapidly ($c\tau = 25$ nm) into two photons and have to be reassembled in later stages of the reconstruction.

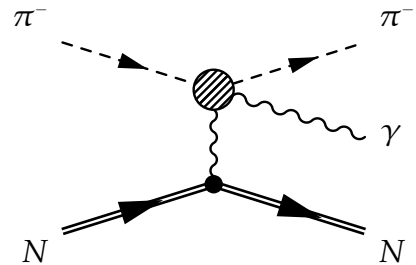
The energy of incident hadrons is measured in the hadronic calorimeters. As this measurement only has an energy resolution of about 5% it cannot be used to distinguish pions from kaons. This is therefore done by the RICH. Since the decay length¹⁰ of a K_s is only 27 mm it will decay inside the detector even at the highest COMPASS energy of 190 GeV. Thus it also has to be reassembled in later stages of the reconstruction. The K_L decay length is 15.5 m making it approximately stable inside the detector. Therefore it is seen only in the hadronic calorimeter.

¹⁰Lifetime times speed of light. This has to be multiplied with the time dilatation to get the actual reach.

Chapter 3

Primakoff Scattering

The term Primakoff scattering means the reaction depicted in the right hand figure. The kinematics of the $2 \rightarrow 3$ reaction is discussed in the section 3.2 and the energy distribution of the exchanged photon is derived in section 3.3. This photon will by virtue of the Primakoff mechanism (cf. section 3.5) be considered external to the vertex of the actual Compton scattering, which is connected to the polarizabilities $\bar{\alpha}$ and $\bar{\beta}$ in section 3.4. All these parts will be combined to yield the scattering cross section found in section 3.6. Section 3.7 summarizes theoretical predictions and previous measurements. All relations are given assuming $\hbar = c = 1$, thus $e^2 = 4\pi\alpha$.



3.1 Polarizabilities of hadrons

Polarizability in the classical sense means that a dipole moment can be induced by applying an external field. If e.g. a Hydrogen atom is put into an electric field the proton and the electron will be subject to forces in opposite directions, thereby displacing the two by a short distance and creating an electric dipole moment. The ratio of this dipole moment and the external field strength is called polarizability and depends on the strength and range of the forces that bind the two different charges together.

The pion also is a compound object consisting of quarks and gluons. Since there are constituents of different electric charge inside, it is easy to imagine an influence of an electric field similar to the case of the Hydrogen atom, although this picture is quite naïve. Calculations in chiral perturbation theory [B⁺94] and measurements at Crystal Ball [KS92] show that the polarizability of the π^0 is smaller

than that of the charged pions despite the bigger charge difference available in the quark content. The failure of this simple model is due to the different structure of the binding force: the quarks in hadrons are bound by the strong interaction that includes more complex processes like the self-interaction of the exchanged quanta, the gluons.

The polarizabilities enter the list of hadron properties as the next two structure parameters besides charge, mass and magnetic moment. They are needed for the expansion of the Compton scattering amplitude in the photon energy ω up to order ω^2 (cf. [Pet81] and references therein). Because of the form of their terms they were named generalized dipole polarizabilities. For brevity they will be called polarizabilities only. Higher orders of the expansion would require further parameters, e. g. higher multipole polarizabilities.

3.2 The kinematics

The examination of the reaction will take place in two frames: the Weizsäcker-Williams approximation and the Compton cross section will be given in the projectile frame¹ while estimates of angles and energies are mainly of interest in the laboratory frame².

In the following sections mathematical objects will be used that are typeset differently for better readability:

scalars and norms of vectors	M, P
three-vectors	\mathbf{P}
Lorentz-vectors	$\mathbf{P} = (P_E, P_x, P_y, P_z)$
Physical and mathematical constants	$\pi, e(\text{Euler}), i, e(\text{charge}), c, \alpha, \hbar$

3.2.1 In the laboratory frame

The event topology is as follows: the incident π^- with a momentum of about 190 GeV along the beam axis scatters off the target nucleus, producing a photon in the process. The nucleus slowly recoils receiving only a few keV of the energy, while the π^- and the γ share the rest of the initial 190 GeV.

¹outgoing π^- at rest, cf. section 3.2.2

²target nucleus at rest

To simplify the following discussion the coordinate system is rotated so that the incident pion moves along the z axis and no momentum is transferred to the nucleus in y direction. Concerning four-momentum conservation the pion-photon system in the final state is rotational symmetric about the direction of its total momentum. Thus it can also be rotated so that the y components of the momenta of the pion and the photon are zero.

The four-momenta participating in the process are that of the incident pion \mathbf{P} whose mass will be denoted m , the momentum transfer to the nucleus by the virtual photon \mathbf{q} , the outgoing pion \mathbf{p} and the produced photon \mathbf{k} . Since the nucleus of mass M has to absorb the virtual photon, a dispersion relation for \mathbf{q} can be formulated:

$$(M + q_E)^2 - \mathbf{q}^2 = M^2 \quad \Rightarrow \quad \mathbf{q}^2 = -2Mq_E \quad (3.1)$$

Making use of the chosen coordinate system and obeying three-momentum conservation the four-vectors can be written as (cf. fig. 3.3 for an illustration)

$$\begin{aligned} \mathbf{k} &= \begin{pmatrix} \sqrt{k_x^2 + k_z^2} \\ k_x \\ 0 \\ k_z \end{pmatrix} \\ \mathbf{P} &= \begin{pmatrix} \sqrt{m^2 + P^2} \\ 0 \\ 0 \\ P \end{pmatrix} \\ \mathbf{p} &= \begin{pmatrix} \sqrt{m^2 + (k_x + q_x)^2 + (P - q_z - k_z)^2} \\ -k_x - q_x \\ 0 \\ P - q_z - k_z \end{pmatrix} \\ \mathbf{q} &= \begin{pmatrix} \sqrt{M^2 + q_x^2 + q_z^2} - M \\ q_x \\ 0 \\ q_z \end{pmatrix} \end{aligned} \quad (3.2)$$

There are only four kinematic variables in this system: k_x , k_z , q_x and q_z . While three-momentum is inherently conserved the equation for energy conservation has four terms, one of which is exceedingly small: because of the use of the Primakoff method that will be explained in section 3.5 we are interested in small \mathbf{q}^2 , more precisely a cut will be applied so that $|\mathbf{q}^2| < 0.001 \text{ GeV}^2$ (cf. section 5.2). Because of the dispersion relation (3.1) this implies a cut on the energy transfer of $q_E < 2.6 \text{ keV}$. Solving the equation exactly leads to a very bulky expression, which can be significantly simplified by neglecting this term. For the moment let $q_x \equiv 0$, the case of pure longitudinal recoil. To distinguish this from the general

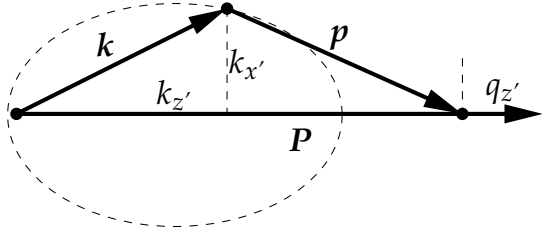


Figure 3.1: kinematics for the longitudinal case. The dashed ellipse is described by eq. (3.3). The plot is not drawn to scale.

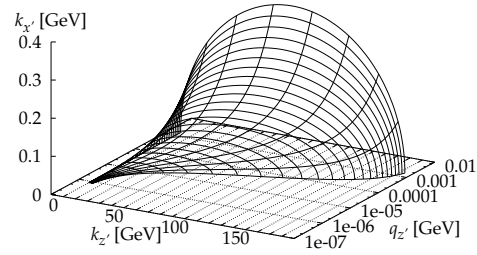


Figure 3.2: allowed photon momenta in the laboratory frame for a given $q_{z'}$ and $q_{x'} = 0$

case the vector components are denoted x' and z' as illustrated in fig. 3.1. The result is

$$k_{z'} = \frac{2P^2 q_{z'} - 3Pq_{z'}^2 + q_{z'}^3 \pm \beta^{-1} P \sqrt{q_{z'}^2 (q_{z'} - 2P)^2 - 4k_{x'}^2 (m^2 + 2Pq_{z'} - q_{z'}^2)}}{2(m^2 + 2Pq_{z'} - q_{z'}^2)} \quad (3.3)$$

For a 190 GeV π^- in the initial state $\gamma = 1360$ and $\beta^{-1} = 1.00000027$. Requiring the square root to be real, which corresponds to the restriction to physically allowed kinematics, yields the relation

$$|k_{x'}| \leq \frac{2Pq_{z'} - q_{z'}^2}{2\sqrt{m^2 + 2Pq_{z'} - q_{z'}^2}} \quad (3.4)$$

For a given $q_{z'}$ eq. (3.3) describes an ellipse centered at the $k_{z'}$ axis, so the maximum and minimum values for $k_{z'}$ are obtained for $k_{x'} = 0$. These are

$$k_{z'}^{\min} = \frac{2P^2 q_{z'} (1 - \beta^{-1}) - Pq_{z'}^2 (3 - \beta^{-1}) + q_{z'}^3}{2(m^2 + 2Pq_{z'} - q_{z'}^2)} \quad (3.5)$$

$$k_{z'}^{\max} = \frac{2P^2 q_{z'} (1 + \beta^{-1}) - Pq_{z'}^2 (3 + \beta^{-1}) + q_{z'}^3}{2(m^2 + 2Pq_{z'} - q_{z'}^2)} \quad (3.6)$$

Fig. 3.2 shows the relation $k_{x'}(k_{z'}, q_{z'})$ for $q_{x'} = 0$. It clearly displays the fact that a specific minimum momentum transfer to the nucleus is required to enable the production of a photon with a given energy in the laboratory frame. This relation will be needed for the integration of the differential cross section. As it enters only logarithmically it is reasonable to use an approximation, exploiting that $q_{z'} \ll P$

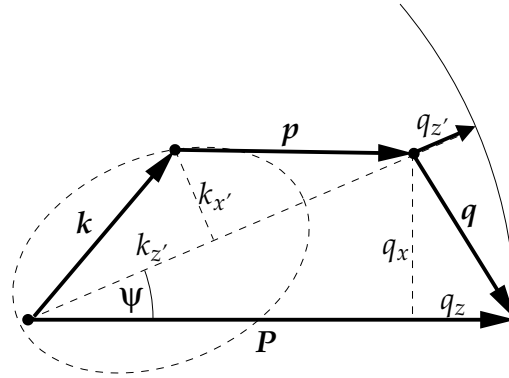


Figure 3.3: kinematics in the general case. The circle has a radius of $|P|$ while the dashed ellipse is the one described by eq. (3.3). The plot is not drawn to scale.

and $\beta^{-1} \approx 1$. In the case of the smallest possible $q_{z'}$ for a certain photon energy the transverse photon momentum $k_{x'} = 0$ (cf. fig. 3.2), so that all momenta are collinear. Application of the approximations results in

$$k_{z'} = \frac{2P^2 q_{z'}}{m^2 + 2Pq_{z'}} \quad \Longrightarrow \quad q_{z'} = \frac{m^2 k_{z'}}{2Pp} \quad (3.7)$$

where $p = P - k_{z'}$ is the momentum of the outgoing pion. As all vectors are collinear the boost to the outgoing pion rest frame³ can be expressed by $\beta\gamma = \frac{p}{m}$ and the photon energy in this reference frame is $\omega = \frac{k}{(1+\beta)\gamma}$. Since the desired relation will only be used for $p > 10$ GeV again $\beta \approx 1$ and the result is

$$q_{\min}^2 = -\left(\frac{m\omega}{P}\right)^2 \quad (3.8)$$

As stated above, ω is the photon energy in the rest frame of the outgoing pion while P is the momentum of the incoming pion in the laboratory reference frame. Application of the same approximation $q_{z'} \ll P$ and $\beta^{-1} \approx 1$ to eq. (3.4) yields

$$k_{x'} = \frac{Pq_{z'}}{\sqrt{m^2 + 2Pq_{z'}}} \quad (3.9)$$

For small $q_{z'}$ this is $\frac{Pq_{z'}}{m}$, while for big $q_{z'}$ it is $\sqrt{\frac{1}{2}Pq_{z'}}$, the scale is given by $\frac{m^2}{2P} = 52$ keV. On the same scale $k_{z'}$ as given in eq. (3.7) is proportional to $q_{z'}$ for small $q_{z'}$ and approaches P for big $q_{z'}$. Since the detection of the photon requires that its energy exceeds a certain threshold its maximum polar angle is

³this will be explained in the next section

3 PRIMAKOFF SCATTERING

limited and reaches a maximum for the biggest allowed value for $q_{z'}$. For a detection threshold of half of the beam energy and a maximum momentum transfer of $-q^2 = 1000 \text{ MeV}^2$ the tangent of this angle is given by the ratio

$$\tan \theta = \frac{2k_{x'}}{P} \approx \sqrt{\frac{2q_{z'}}{P}} \quad (3.10)$$

This evaluates to 18 mrad in the case of 190 GeV beam energy. However, as we will see the cross section decreases as q^{-4} , so these big angles are extremely rare. It will therefore be sufficient to test angles up to 10 mrad.

It has to be noted that $q_{z'}$ is limited by two constraints. First the approximation that led to eq. (3.3) is only valid if the energy transfer to the nucleus is negligible compared to the other particles' energies. Second, there is a limit on the maximum q^2 that is transferred by a photon. If the pion directly hits the nucleus, i. e. if the impact parameter⁴ is smaller than the radius of the nucleus, it will interact with a single nucleon via the strong interaction. According to [PDG00] the hadronic cross section of Lead is 1.77 barn; the radius of the corresponding circular area is 7.5 fm. The relation between the impact parameter b and the momentum transfer q for small angles is (see [MK84])

$$q = \frac{Ze^2}{b} \quad (3.11)$$

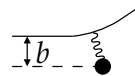
For Lead ($Z = 82$) an impact parameter of 7.5 fm corresponds to a momentum transfer of 198 MeV. This implies that for $-q^2 \gtrsim 0.04 \text{ GeV}^2$ the hadronic interaction dominates the cross section. In turn, the cut $-q^2 < 1000 \text{ MeV}^2$ selects the electromagnetic interaction.

If we consider only the π^- in the initial state and the π^- and γ in the final state it is clear that the invariant mass of the final state is greater than the pion mass.⁵ Thus the incident π^- has to lose momentum to enable the production of a γ . The condition for q following from this constraint is illustrated in fig. 3.3:

$$|\mathbf{p} + \mathbf{k}| < |\mathbf{P}| \quad (3.12)$$

From the figure it is also clear that after rotating the final state until $q_{x'} = 0$ the situation is as the one discussed above since a rotation has no influence on the energy sums and the energy transfer to the nucleus is neglected. After replacing $q_{z'}$ by

⁴shortest distance between the classical particle's initial direction and the center of the nucleus:



⁵In the center of mass system of the $\pi^- \gamma$ final state the total energy—in this system also the invariant mass—in terms of the photon energy k is $E = k + \sqrt{m_\pi^2 + k^2} > m_\pi$

$$q'_z = P - \sqrt{(P - q_z)^2 + q_x^2} \quad (3.13)$$

and rotating the momenta of the outgoing particles by the angle ψ eq. (3.3) can also be used to calculate the general case. As $q_{z'} \leq q_z$ the transverse momentum transfer does not only change the direction of the particles in the final state, it also makes the ellipse of possible photon momenta smaller. The biggest rotation of the final state happens when $q_{z'}$ is just big enough to produce a photon whose energy matches the detection threshold and the rest of the allowed q^2 is used up by the transverse momentum transfer. As in this case the longitudinal components are small compared to the transverse ones the ratio of the maximum momentum transfer and the beam energy equals the tangent of the rotation angle

$$\tan \psi = \frac{\sqrt{-q_{\text{max}}^2}}{P} \quad (3.14)$$

This evaluates to $166 \mu\text{rad}$ if $-q_{\text{max}}^2 = 1000 \text{ MeV}^2$ and $P = 190 \text{ GeV}$ and is small compared to the pion and photon angles that occur in the longitudinal case.

3.2.2 In the projectile frame

Primakoff scattering is described as Compton scattering in inverse kinematics. This means that the CPT ⁶ inverted process is considered: the scattering of a real photon by a pion at rest into the recoiling pion and a virtual photon which is absorbed by a nucleus. It is therefore advantageous to calculate the observables in the rest frame of the outgoing pion. Throughout this thesis the term projectile frame thus refers to the rest frame of the *outgoing* pion.

Given the momentum $p = \beta\gamma mc$ and polar angle ϕ of the outgoing pion in the laboratory frame the transformation from the projectile frame to the laboratory is

$$T = \begin{pmatrix} 1 & 0 & 0 & 0 \\ 0 & \cos \phi & 0 & -\sin \phi \\ 0 & 0 & 1 & 0 \\ 0 & \sin \phi & 0 & \cos \phi \end{pmatrix} \cdot \begin{pmatrix} \gamma & 0 & 0 & \beta\gamma \\ 0 & 1 & 0 & 0 \\ 0 & 0 & 1 & 0 \\ \beta\gamma & 0 & 0 & \gamma \end{pmatrix} \quad (3.15)$$

The cross section will be given in terms of the photon energy ω and polar angle θ in the projectile frame. Because of the \mathcal{P} transformation the direction of the z axis is inverted. Thus the polar angle also has to be transformed by $\theta \rightarrow \pi - \theta$, which

⁶ C : charge conjugation, transforms particles into their anti-particles

\mathcal{P} : parity, inverts all vectors as $x \rightarrow -x$

T : time reversal, replaces $t \rightarrow -t$

3 PRIMAKOFF SCATTERING

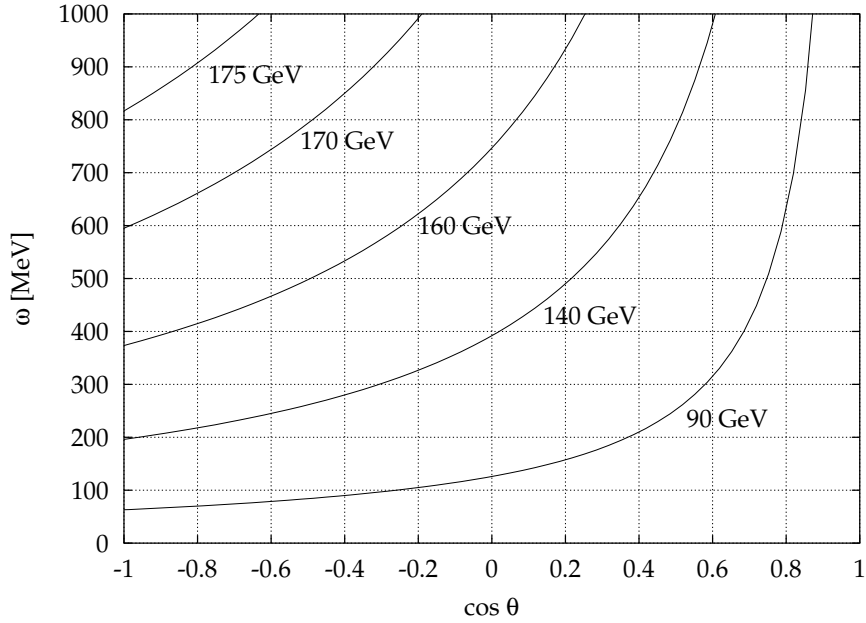


Figure 3.4: photon energy in the laboratory frame (numbers on the curves) corresponding to energy and angle of the photon in the projectile frame

leads to a sign inversion for $\cos \theta$. With this knowledge the relation between the observables in the projectile frame and the photon energy k in the laboratory is

$$k = \gamma\omega - \beta\gamma\omega \cos \theta \quad (3.16)$$

where the boost depends on the energy of the outgoing pion in the laboratory frame as (energy transfer to the nucleus neglected)

$$\beta\gamma = \frac{P - k}{m} \quad (3.17)$$

Combining the two equations yields

$$k = \frac{P}{1 + \frac{m}{\beta\omega(1 - \cos\theta)}} \quad (3.18)$$

Fig. 3.4 illustrates this relation. It shows which cut in the photon energy/angle plane is introduced by a cut on the photon energy in the laboratory frame.

3.2.3 Mandelstam variables

For the calculation of the Compton cross section some Mandelstam variables are used. Since section 3.4 will only be concerned with the process $\pi^- \gamma \rightarrow \pi^- \gamma$ it will use the usual four-vectors \mathbf{p} , \mathbf{p}' , \mathbf{k} and \mathbf{k}' for the momenta \mathbf{P} , \mathbf{p} , \mathbf{q} and \mathbf{k} . As illustrated in fig. 3.6 the three mandelstam variables are

$$\begin{aligned} s_1 &= (\mathbf{P} + \mathbf{q})^2 \hat{=} (\mathbf{p} + \mathbf{k})^2 \\ s_2 &= (\mathbf{P} - \mathbf{k})^2 \hat{=} (\mathbf{p} - \mathbf{k}')^2 \\ t &= (\mathbf{P} + \mathbf{p})^2 \hat{=} (\mathbf{p} + \mathbf{p}')^2 \end{aligned} \quad (3.19)$$

3.3 The Weizsäcker-Williams approximation

This section summarizes the derivation of the Weizsäcker-Williams approximation as elaborated in [Hei54]. It illustrates the idea and shows how to calculate it semi-classically. Following [Bué95] the result of an equivalent covariant derivation given in [PS61] will be used in the following calculations.

3.3.1 Semi-classical

The field of a highly relativistic point charge looks similar to that of a set of light waves. When such a field acts upon a particle at rest, one of these photons, \mathbf{k} , may be scattered by the particle at rest into another state \mathbf{k}' . The photon \mathbf{k} is removed from the energy spectrum of the fast particle, while the particle at rest receives the recoil $\mathbf{k} - \mathbf{k}'$. The cross section for this process is that for scattering of the photon \mathbf{k} by the particle at rest multiplied by the number of photons in the state \mathbf{k} .

For this method to be applicable the motion of the fast particle must practically remain a straight line during the process. This condition is fulfilled in the projectile frame where a very fast nucleus with 27–283 TeV total energy exchanges a photon of less than 1 GeV transverse momentum with a pion at rest.

The first step is to calculate the field of a fast moving point charge using retarded potentials⁷. An analysis of the frequencies present in the field shows that the electric and magnetic fields are indeed in the relationship corresponding to a plane light wave. Integration of the energy density over the impact parameter yields the following photon spectrum shown in fig. 3.5:

⁷see e. g. [Fli97] for a discussion

3 PRIMAKOFF SCATTERING

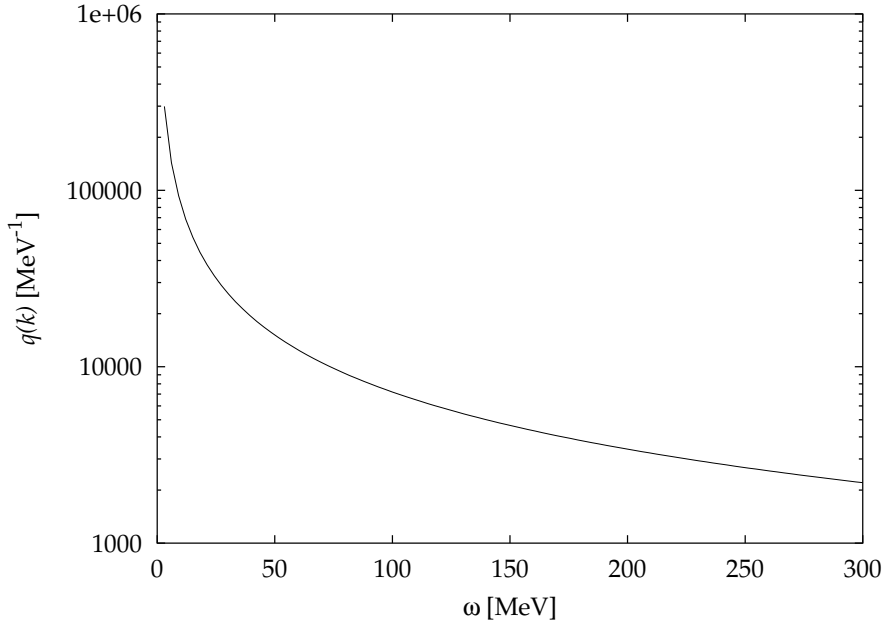


Figure 3.5: the energy spectrum of the virtual photons constituting the electric field of a 100 TeV Lead nucleus

$$q(\omega) d\omega = \frac{\pi Z^2 e^2}{2} \frac{d\omega}{\hbar c} \frac{1}{\omega} \left[\log \frac{E}{\omega} - 0.38 \right], \quad \frac{M\omega}{mE} \ll 1 \quad (3.20)$$

For the present reaction the mass of the Lead nucleus is $M = 193 \text{ GeV}$, the pion mass is $m = 140 \text{ MeV}$, $E = 27 - 283 \text{ TeV}$ and $\omega < 1 \text{ GeV}$ the condition to the right is obviously true.

3.3.2 Covariant

As derived in [PS61] the cross section for bremsstrahlung of a hadron of mass m in the field of a nucleus with charge Ze is

$$\frac{d^3\sigma}{dq^2 ds_1 d\cos\theta} = \frac{\alpha}{\pi} \frac{Z^2}{s_1 - m^2} \frac{q^2 - q_{\min}^2}{q^4} |F_A(q^2)|^2 \frac{d\sigma_{\text{Compton}}(s_1, \cos\theta)}{d\cos\theta} \quad (3.21)$$

or equivalently in terms of the incident⁸ photon energy ω in the projectile frame

$$\frac{d^3\sigma}{dq^2 d\omega d\cos\theta} = \frac{\alpha}{\pi} \frac{Z^2}{\omega} \frac{q^2 - q_{\min}^2}{q^4} |F_A(q^2)|^2 \frac{d\sigma_{\text{Compton}}(\omega, \cos\theta)}{d\cos\theta} \quad (3.22)$$

⁸The incident photon in the projectile frame is the outgoing photon in the laboratory frame, cf. section 3.2.2.

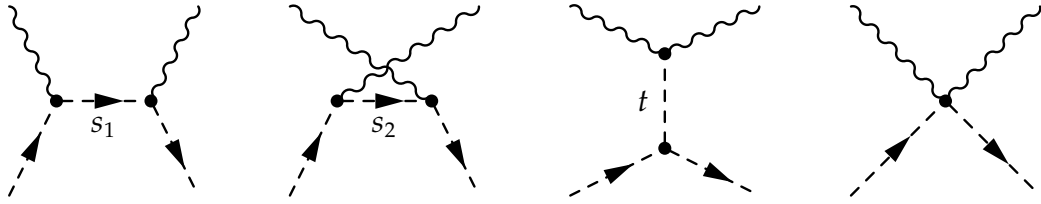


Figure 3.6: tree level diagrams contributing to the Compton amplitude

where σ_{Compton} is the cross section for Compton scattering. $F_A(t)$ is the electromagnetic form factor of the nucleus which is approximately 1 for the q^2 range considered.

3.4 Low energy theorems in QED

This section introduces the polarizability parameters and gives the form of the Compton scattering cross section of low-energy photons on a zero-spin non-pointlike particle. It is mainly a summary of an article by V. A. Petrunkin [Pet64].

At tree level the four diagrams shown in fig. 3.6 contribute to the Compton cross section. The left two describe photon absorption and emission, the third is the exchange term with the dashed line representing some massive boson and the fourth is the contact term. Representing the pion by the charged Bose field operator $\Phi(x)$ and the corresponding total current operator $j(x)$, the S matrix is

$$\begin{aligned} \langle p'k'\epsilon'|S|pk\epsilon\rangle &= -\frac{2ie^2}{\sqrt{4\omega\omega'}} \langle p'|(\epsilon \cdot \epsilon') \int \Phi^*(\mathbf{x})\Phi(\mathbf{x}) \exp [i(\mathbf{k} - \mathbf{k}')\mathbf{x}] d\mathbf{x} |p\rangle \\ &\quad - \frac{1}{\sqrt{4\omega\omega'}} \langle p'| \int P \left[(j(\mathbf{x}) \cdot \epsilon') (j(\mathbf{y}) \cdot \epsilon) \right] \exp [i(\mathbf{k}\mathbf{y} - \mathbf{k}'\mathbf{x})] d\mathbf{x} d\mathbf{y} |p\rangle \end{aligned} \quad (3.23)$$

P is Dyson's time ordering operator, k, p, k', p' are the four-momenta of the photon and particle in the initial and final states and ϵ and ϵ' are the photon polarizations. The first term corresponds to the contact interaction while the second term includes the three other graphs. A parametrization of this matrix element was introduced by Low [Low54]

$$\langle |S| \rangle = -\frac{\epsilon'_i \epsilon_j g_{ij}}{\sqrt{4\omega\omega'}} \quad (3.24)$$

where the dynamics of the scattering process is contained in the tensor g_{ij} ($i = 1, 2, 3$)—not to be confused with the relativistic metric $g_{\mu\nu}$. After going over to

3 PRIMAKOFF SCATTERING

time-independent operators, performing the integration over t , summing over all possible intermediate states and using one of Low's relations one obtains

$$k'_i g_{ij} k_j = i(2\pi)^4 \delta(\mathbf{p}' + \mathbf{k}' - \mathbf{p} - \mathbf{k}) \omega \omega' \left\{ \frac{e^2}{\sqrt{mE}} \left[\cos \theta + \frac{1}{4} \left(\frac{\omega}{m} \right)^2 + \frac{1}{4} \left(\frac{\omega}{m} \right)^2 \cos \theta - \frac{1}{3} \omega^2 \langle r^2 \rangle \cos \theta - \frac{1}{2} \left(\frac{\omega}{m} \right)^2 \cos^2 \theta \right] - \bar{\alpha} \omega^2 \cos \theta \right\} \quad (3.25)$$

where m and E are the particle's energies before and after the interaction, $\langle r^2 \rangle$ is the second moment of the charge distribution and $\bar{\alpha}$ is a new parameter. To determine the explicit form of g_{ij} it is necessary to construct the general form of the S matrix by proceeding from Lorentz and gauge invariance:

$$\langle |S| \rangle = - \frac{(2\pi)^4 i \delta(\mathbf{p}' + \mathbf{k}' - \mathbf{p} - \mathbf{k})}{4\sqrt{\omega \omega' m E}} (D_1 I_1 + D_2 I_2) \quad (3.26)$$

I_1 and I_2 are constructed from ϵ , ϵ' , \mathbf{k} , \mathbf{k}' and $\Delta = (\mathbf{p} + \mathbf{p}')^2$ to satisfy Lorentz and gauge invariance as well as the crossing symmetry⁹. D_1 and D_2 contain the dynamics of the scattering process and are scalar functions of the invariants $s_1 = (\mathbf{p} + \mathbf{k})^2$, $s_2 = (\mathbf{p} - \mathbf{k}')^2$ and $t = (\mathbf{p} + \mathbf{p}')^2 = (\mathbf{k} + \mathbf{k}')^2$. To isolate the poles of the first two graphs in fig. 3.6 it is assumed that D_2 is of the form

$$D_2 = \frac{D'_2}{(s_1 - m^2)(s_2 - m^2)} \quad (3.27)$$

Evaluating the S matrix in the projectile frame and expanding D_1 and D'_2 in the neighborhood of the pole $s_1 = s_2 = m^2$ and $t = 0$ yields

$$\begin{aligned} D_1 &= D_{01} + (D_{11} + D_{21} \cos \theta) \omega \omega' + \mathcal{O}(\omega^4) \\ D'_2 &= D_{02} + (D_{12} + D_{22} \cos \theta) \omega \omega' + \mathcal{O}(\omega^4) \end{aligned} \quad (3.28)$$

$$\begin{aligned} D_{01} &= D_{02} = 2e^2 & D_{11} &= -2m\bar{\alpha} \\ D_{21} &= D_{12} + 2m\bar{\alpha} = -2m\bar{\beta} & D_{22} &= 0 \end{aligned} \quad (3.29)$$

The parameters $\bar{\alpha}$ and $\bar{\beta}$ are the electric and magnetic dipole polarizabilities of the particle. Finally, the matrix element in the rest frame of the outgoing particle is

⁹This symmetry means that the S matrix is invariant under the exchange of an incoming and an outgoing particle if their four-momenta simultaneously are inverted.

$$\langle |S| \rangle = -\frac{(2\pi)^4 i \delta(\mathbf{p}' + \mathbf{k}' - \mathbf{p} - \mathbf{k})}{4\sqrt{\omega\omega' m E}} \left\{ \left(\frac{e^2}{m} - \omega\omega'\bar{\alpha} \right) (\boldsymbol{\epsilon} \cdot \boldsymbol{\epsilon}') - \bar{\beta} (\boldsymbol{\epsilon} \times \mathbf{k})(\boldsymbol{\epsilon}' \times \mathbf{k}') \right\} \quad (3.30)$$

The polarizability terms are enhanced by a factor of $\omega\omega'$ compared to the Thompson term $\frac{e^2}{m}(\boldsymbol{\epsilon} \cdot \boldsymbol{\epsilon}')$, so though the parameters $\bar{\alpha}$ and $\bar{\beta}$ are small the effect grows with photon energy. For collinear scattering the polarization vector does not change. Thus in the case of forward scattering ($\mathbf{k}' = \mathbf{k}$) the polarizability effect is proportional to $\bar{\alpha} + \bar{\beta}$ while for backscattering ($\mathbf{k}' = -\mathbf{k}$) it is proportional to $\bar{\alpha} - \bar{\beta}$. If $\bar{\alpha} - \bar{\beta} > 0$ and $\bar{\alpha} + \bar{\beta} > 0$ the polarizability effect results in a smaller cross section compared to the Compton amplitude for pointlike pions.

3.5 The Primakoff mechanism

While there are many possibilities for a π^- to interact with a nucleus and produce the discussed final state only the single-photon exchange has a pole at $q^2 = 0$. Therefore the scattering amplitude can be split into two parts for very small q^2 :

$$F(q^2) = \frac{F(0)}{q^4} + \text{const} \quad (3.31)$$

Because of the steep rise of the first part in the vicinity of the real photon case ($q^2 = 0$) a fit to data taken in this range will naturally extrapolate from slightly virtual to quasi-real photons. This behaviour permits the measurement of quasi-real particle properties with the virtual photons of the electromagnetic field of a nucleus (cf. [Pri51]).

3.6 Combining the ingredients

Evaluating eq. (3.22) and eq. (3.30) yields

$$\frac{d^3\sigma}{dq^2 d\omega d\cos\theta} = \frac{\alpha^2 Z^2 (q^2 - q_{\min}^2)}{mq^4} f(\omega, \cos\theta) \quad (3.32)$$

As q^2 will not be measured the corresponding term has to be integrated:

$$\int_{q_{\min}^2}^{q_{\max}^2} \frac{q^2 - q_{\min}^2}{q^4} dq^2 = \ln \frac{q_{\max}^2}{q_{\min}^2} - 1 + \frac{q_{\min}^2}{q_{\max}^2} \quad (3.33)$$

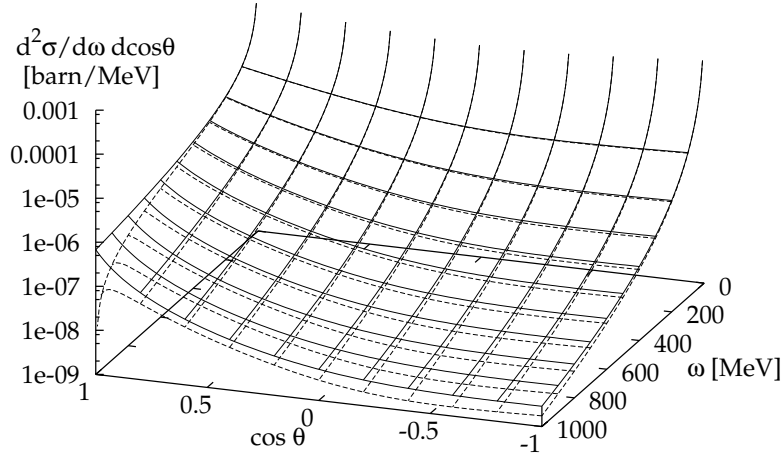


Figure 3.7: calculated cross section in the projectile frame for $\bar{\alpha} = \bar{\beta} = 0$ (solid) and $\bar{\alpha} = 7 \cdot 10^{-4} \text{ fm}^3$, $\bar{\beta} = -6 \cdot 10^{-4} \text{ fm}^3$ (dashed)

Calculating q_{\min}^2 according to eq. (3.8) the resulting differential cross section is

$$\frac{d^2\sigma}{d\omega d\cos\theta} = \frac{\alpha^2 Z^2}{m} \left(\ln \frac{-q_{\max}^2 P^2}{em^2\omega^2} - \frac{m^2\omega^2}{q_{\max}^2 P^2} \right) \cdot \left\{ \frac{\alpha}{m\omega} \frac{1 + \cos^2\theta}{\left[1 + \frac{\omega}{m}(1 - \cos\theta)\right]^2} - 2\omega \frac{\bar{\alpha}(1 + \cos^2\theta) + 2\bar{\beta}\cos\theta}{\left[1 + \frac{\omega}{m}(1 - \cos\theta)\right]^3} \right\} \quad (3.34)$$

The cross section is plotted in fig. 3.7. Higher order terms of the polarizabilities were omitted because of the smallness of these parameters. Furthermore the well-known relation for Compton scattering was used to eliminate ω' :

$$\omega' = \frac{\omega}{1 + \frac{\omega}{m}(1 - \cos\theta)} \quad (3.35)$$

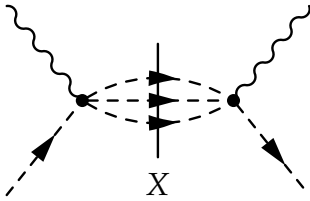
3.7 Predictions and Measurements

From the optical theorem, the expansion of the forward Compton amplitude in orders of ω and the Kramers-Kronig relations¹⁰ Baldin's sum rule [Bal60] is ob-

¹⁰see e. g. [Fl97]

tained:

$$\bar{\alpha} + \bar{\beta} = \frac{1}{2\pi^2} \int_{\omega_0}^{\infty} \frac{\sigma(\omega') d\omega'}{\omega'^2} \quad (3.36)$$



The cross section $\sigma(\omega)$ consists of all graphs of the type shown in the left hand figure where contributions to $\bar{\alpha} + \bar{\beta}$ are only obtained for graphs where the intermediate state X contains more than a pion. Since the first excited state, a second pion in the intermediate state, is suppressed by the chiral anomaly, the factor ω^{-2} leads to a very small value for $\bar{\alpha} + \bar{\beta}$.

It depends on the publication whether $\bar{\alpha}$ and $\bar{\beta}$ are given or linear combinations thereof, thus for better comparison $\bar{\alpha} + \bar{\beta}$ and $\bar{\alpha} - \bar{\beta}$ will be presented too. It will be shown in section 5.4 that the polarizabilities are highly correlated in the measurement, so the errors given for derived observables, that are calculated by adding the individual errors in quadrature, will almost certainly be over-estimated. Therefore the corresponding lines will be marked with a *. If only one error is given no distinction had been made between statistical and systematic errors, otherwise the statistical error is given first.

From the measurement at Serpukhov [A⁺85] the following values were found:

$$\begin{aligned} \bar{\alpha} + \bar{\beta} &= (1.4 \pm 3.1 \pm 2.5) \cdot 10^{-4} \text{ fm}^3 \\ \bar{\alpha} - \bar{\beta} &= (15.6 \pm 6.4 \pm 4.4) \cdot 10^{-4} \text{ fm}^3 & * \\ \bar{\alpha} &= (5.7 \pm 4.2 \pm 3.1) \cdot 10^{-4} \text{ fm}^3 & * \\ \bar{\beta} &= (-7.1 \pm 2.8 \pm 1.8) \cdot 10^{-4} \text{ fm}^3 \end{aligned}$$

Another analysis of the Serpukhov data by [Bué95] comes to the conclusion

$$\begin{aligned} \bar{\alpha} + \bar{\beta} &= (1.1 \pm 2.6) \cdot 10^{-4} \text{ fm}^3 & * \\ \bar{\alpha} - \bar{\beta} &= (12.3 \pm 2.6) \cdot 10^{-4} \text{ fm}^3 & * \\ \bar{\alpha} &= (5.6 \pm 1.6) \cdot 10^{-4} \text{ fm}^3 \\ \bar{\beta} &= (-6.7 \pm 2.0) \cdot 10^{-4} \text{ fm}^3 \end{aligned}$$

3 PRIMAKOFF SCATTERING

The theoretical calculations of [Bür96] yield

$$\begin{aligned}\bar{\alpha} + \bar{\beta} &= (0.3 \pm 0.1) \cdot 10^{-4} \text{ fm}^3 \\ \bar{\alpha} - \bar{\beta} &= (4.4 \pm 1.0) \cdot 10^{-4} \text{ fm}^3 \\ \bar{\alpha} &= (2.4 \pm 0.5) \cdot 10^{-4} \text{ fm}^3 \\ \bar{\beta} &= (-2.1 \pm 0.5) \cdot 10^{-4} \text{ fm}^3\end{aligned}$$

In that paper also the data of CELLO [CE92] and Mark II [Ma90] is analyzed. These experiments examined the process $\gamma\gamma \rightarrow \pi^+\pi^-$ which is equivalent to Compton scattering because of the crossing symmetry. These experiments confirm the smallness of $\bar{\alpha} + \bar{\beta}$, but they contradict the Serpukhov result for $\bar{\alpha} - \bar{\beta}$:

$$\begin{aligned}\bar{\alpha} + \bar{\beta} &= \begin{cases} (0.22 \pm 0.07 \pm 0.04) \cdot 10^{-4} \text{ fm}^3 & \text{[Mark II]} \\ (0.33 \pm 0.06 \pm 0.01) \cdot 10^{-4} \text{ fm}^3 & \text{[CELLO]} \end{cases} \\ \bar{\alpha} - \bar{\beta} &= (4.8 \pm 1.0) \cdot 10^{-4} \text{ fm}^3 \\ \bar{\alpha} &= \begin{cases} (2.5 \pm 1.0) \cdot 10^{-4} \text{ fm}^3 & \text{[Mark II]} \\ (2.6 \pm 1.0) \cdot 10^{-4} \text{ fm}^3 & \text{[CELLO]} \end{cases} \quad * \\ \bar{\beta} &= (-2.3 \pm 1.0) \cdot 10^{-4} \text{ fm}^3 \quad *\end{aligned}$$

Chapter 4

The Monte Carlo Setup

The following chapter describes the programs and techniques used to perform the simulation. After a short introduction the next two sections introduce the software packages for event generation and particle tracking. The fourth section is dedicated to the COMPASS reconstruction software while the fifth section elaborates the programs used to analyze the results. Before discussing the actual Primakoff studies in the next chapter, various tests of the setup and the software chain are presented.

4.1 The general idea

As outlined in the introduction the Monte Carlo method will be employed to learn more about the COMPASS spectrometer. This requires three prerequisites: a detailed description of the problem, an algorithm for the simulation and a realization in hard- and software.

The problem consists of two parts. First the physical event that is to be studied must be described as precise as possible. This has in part been done in chapter 3. Missing there is the issue of physical background, i. e. other physical processes that produce the same or a very similar final state. As this is a very involving problem please consult [Fri] for further information. Since this simulation shall answer the question of feasibility of the measurement at COMPASS the second part of the problem is the description of the COMPASS spectrometer. The description used is shown graphically in appendix C.

The simulation follows the steps of the process seen in the experiment. First the physical event happens. This step is modeled by a program that pseudo-

4 THE MONTE CARLO SETUP

randomly¹ chooses physically correct kinematics for the final state in a way that after doing this many times the behavior of the underlying physical process is approximated. Next the produced particles move through the apparatus, interacting with the material they traverse and leaving traces in the detectors. This step is modeled by another program that moves the particles stepwise through the spectrometer, pseudo-randomly deciding if, where and how the particles interact, thereby sometimes destroying them—like a photon in pair production—or producing secondary particles. When a particle traverses a detector it might leave a trace that is recorded like in the experiment and written to a file so that in the last step the reconstruction software can try to associate these hits again with the crossing of particles. In other words the simulation determines how the real apparatus would have seen that particular physical event. The last step is to determine from the distribution of the reconstructed events the parameters that are to be measured.

The individual software packages mentioned above are described in the next sections while more information about the hardware they run on is presented in appendix A. To maximize the efficiency of the process software and hardware have to be suited to each other. Because of the enormous amounts of data that will be taken by COMPASS the simulation had to be done for about eight million events, resulting in more than 2TB of data. The cheapest way to buy enough computing power was to build a cluster of 32 simple PCs by connecting them with a network. This way the software could run in parallel, thereby roughly dividing the execution time by the number of jobs. Since every PC had two processors the number of jobs was 64.

In consideration of the size of the intermediate files copying them over the network was impractical. To speed up the simulation process the principle of data locality was implemented as far as possible. This means that all intermediate data files were kept locally on the computing nodes and only the end products—the histograms—were transferred to the server.

¹A computer is a deterministic device with no inherent randomness. The usual sources of entropy used for the generation of random numbers are all external like the movement of the mouse or the timing of the keystrokes. Higher rates can be gained from radioactive sources, but still this is not fast enough. Modern computers are so fast that they need at least several thousand random numbers per second. A solution sufficient for Monte Carlo methods to work is to use pseudo-random numbers that are calculated deterministically in such a complex way that they seem to be random.

4.2 The event generators

The first program in the simulation chain is the event generator. This program generates the physical event and writes it to disk in a format readable by the tracking code. Every event consists of a number of particles emerging from a vertex with specific momenta. This makes up one integer for the number, three floating point values for the vertex position and another three floating point values per particle for the momentum information. As input to COMgeant² two file formats are permitted: the numbers can either be stored in binary form or as ASCII strings.

4.2.1 Single particle generator

For testing the simulation chain a self-written generator was used to produce single particle events (see appendix B). Like all other programs it makes use of the CERNLIB³ random number generators. The details of the events produced are specified via command line parameters. These are the particle type, the momentum range, the range in the polar angle θ and the number of events. The azimuthal angle is always randomized in the range $[0, 2\pi)$ while for θ randomization two models are selectable: to achieve a homogenous distribution in momentum space, $\cos \theta$ is randomized, while for test purposes a flat θ distribution can be produced.

This generator was used to test the detector description as will be explained in section 4.6 to generate pion and photon events with energy ranging from 1–200 GeV and angles in the range of 0–10 mrad. Its output format is the ASCII text file.

4.2.2 Polaris

This Primakoff scattering generator was written by V. Steiner (Tel Aviv University) in 1995 and was used for the simulations published in [Bué95]. It was modified to write only the hard events with scattered pion energy below 100 GeV to the output file.

The parameters are passed to the program via a configuration file that is read at startup. The target material as well as the pion polarizabilities and the number of events can be controlled together with further settings that were not touched

²see next section

³CERN library for high energy physics

during the simulation. For these parameters the defaults from the CERN `simevt` package were used. This generator does not simulate beam divergence or momentum spread. All events are calculated for a fixed beam energy that was set to 190 GeV.

To be readable by COMgeant the output of Polaris had to be converted to the format described above. The existing converter not only adapts the data to the desired format but also rotates the events by randomized angles to simulate a beam divergence of $0.3 \times 0.6 \text{ mrad}^2$. The energy of the beam particle is also smeared out but this modification is not important as only the beam direction is used in the reconstruction.

4.2.3 Fritiof

For background studies the widely used Fritiof generator was used. It was configured to produce minimum bias events for pion nucleus interaction. This means that the whole range of physical reactions via strong interaction between the π^- and the nucleus is modeled in order to get a good impression how real experimental data will look like. For further detail concerning the theoretical model used in this generator please consult [Fri]. Since it is the design goal of COMPASS to acquire high statistics first, and sort out the good ones later, the question of a good software filter is most interesting.

As this generator is part of the COMgeant executable its output doesn't show up directly in any file. However, the information can be extracted from the COMgeant output.

4.3 Particle tracking

The detector simulation was done by COMgeant [Gea], the COMPASS adaption of the GEANT package. It is an interface program to GEANT 3.21 which was developed for the WA89 experiment (and first called OMgeant). GEANT was also developed at CERN and is used in many places, also outside of the high energy physics community. COMgeant includes plug-ins for the modeling of the RICH detector and the calorimeters. The geometry of the apparatus and the interactions to be simulated are controlled via human readable text files.

The detector definition is constructed using a hierarchy of volumes that are filled with media. The physical properties of a volume are given by the definition of

the medium. These properties include density, radiation length⁴, transparency for magnetic fields, sensitivity to the passing of ionizing particles etc. The shape of a volume can be a box or a tube. For the active areas the positions of readout strips and the time resolution have to be specified.

From these primitives the detector stations are constructed, e. g. a box filled with gas, which has a sensitive subvolume and wires in vertical direction would be a very simple model of a detector using gas amplification. The real description is much more detailed to simulate effects of mountings, shieldings and readout electronics on passing particles. These effects will be visible e. g. in the distribution of photon conversion vertices (fig. 4.16 on page 48).

The setup used for the simulation was the official setup for the year 2001 run with the addition of three GEM stations and six silicon stations as projected for the year 2002 run. These were used to complete the tracking stations described in section 2.2.5. Further details about the setup are given in appendix C.

Tracking the particles through the setup is done in steps. The step size is chosen automatically so that the integration of the equations of motion can efficiently be done with sufficient accuracy. Thereby it is limited by the occurrence of discrete physical processes like decay or hard bremsstrahlung, by the crossing of medium boundaries and by the accumulation of momentum change due to continuous processes like multiple scattering or the deflection in a magnetic field. The limits between continuous and discrete processes can be set in the configuration files. For example bremsstrahlung with single photon energy less than 500 keV was accounted for by a continuous approximation. At the beginning of each step the occurrence of a discrete process is pseudo-randomly determined and the rest of the step size limits is calculated. The particle is then moved to its new position, changing the momentum as described by the equations of motion. When traversing a sensitive volume a hit is recorded in the corresponding detector. In the case of a discrete process the interaction takes place at the new position, thereby destroying the particle and possibly creating new ones. After all particles have been moved this way the cycle starts. When all particles are destroyed or have left the setup the simulation of one event is complete. In analogy to the real experiment a number of events that are saved to the same set of files is called a run.

At the end of the run the state of the pseudo-random number generator is saved to disk. This way the next run will continue the series of random numbers, so that each run is unique⁵ and successive runs can be added to increase the statistics.

⁴The distance X_0 a high energy electron has to travel to lose all but e^{-1} of its initial energy by bremsstrahlung only. High energy photons convert into e^+e^- -pairs; the distance such a photon can travel with a survival probability of e^{-1} is approximately $\frac{7}{9}X_0$.

⁵The pseudo-random number generator has a period of 10^{43} so it takes a huge number of runs

The output of COMgeant is a ZEBRA [ZEB] file. ZEBRA is a Fortran library that permits saving and restoring the contents of a set of variables to and from a data file. This file sequentially contains the data of all events that are processed in one run. The present author wrote a program to extract interesting events or to concatenate several files. Based on the documentation of the file format a set of C++ classes was written to be able to read and write single events. This program can also be used to count the events in one file.

The ZEBRA file contains only information on the traces left by particles in detectors. These are referenced by numbers while the geometry of the apparatus is passed in another file. This file is human readable ASCII text and provides an easy way to check the detector positions, wire directions, calorimeter structure etc.

4.4 COMPASS reconstruction software

CORAL is the name of the COMPASS reconstruction and analysis library. It is developed in parallel with the evolution of the experiment. Due to this procedure frequent updates of the software package were necessary. After successfully checking the functionality as reported in section 4.6 all analysis has been done with the validated version.

Being a library CORAL is structured as a set of modules. Examples are TraFFiC⁶, the calorimeter package, the RICH package, a ROOT⁷ output package, the detector data decoding package etc. Another input package is used to read the ZEBRA files produced by COMgeant.

The operation of CORAL is controlled by an option file. Here a number of internal parameters can be set. Most important are the names of the input and output files, the output format to use and where to find the detector description.

During track reconstruction with TraFFiC three steps are taken. First track patterns are searched in the four zones⁸ individually. In this step straight paths are assumed inside each zone. As stated in section 2.2 each detector station provides several layers of strips. If the information from one station could be compressed into the full coordinates of the points where particles crossed the pattern recognition would try to find hits lying approximately on straight lines and sort out the rest as noise. However this information is not directly available. Hits of multiple

to get identical results.

⁶Track Finding and Fitting in COMPASS

⁷see next section

⁸see section 2.2.5

planes at different distances from the target would have to be merged raising the problem of accuracy for tracks with a large angle to the beam axis. Furthermore most detectors only give information on the hit positions, so if multiple hits are present it is not possible to decide which hits in different planes belong together.

By looking at a single layer the hits recorded on its strips provide a projection of the point where the particle passed through this plane onto an axis rectangular to the orientation of the strips. If there are more than two planes with equal orientation these planes are searched for hits that lie approximately on a straight line. Because of the variety of tracking detectors there are several projections that yield such straight lines. These track candidates are scanned for tracks consistent in all available projections so that ghosts produced by multiple hits can be mostly sorted out.

The remaining track candidates are joined in the second step by extrapolating from the endpoints through the magnetic fields. If no matching track can be found on the other side of the magnet, this track will be discarded in the analysis because its momentum can only be reconstructed if it is found before and after traversing a magnetic field. In step three the successfully joined tracks are collected and fitted against the actual hit positions.

The procedure for calorimeter reconstruction is somewhat simpler since for each hit only the different cells of one detector have to be considered. When a particle interacts within a calorimeter it produces a shower of secondary particles that propagates through the cells and is measured with photo multipliers. During reconstruction the amplitudes of all cells are searched to find hit clusters. After fitting the assumed form of the shower to the amplitudes in a the cells of a cluster, a first estimate of the deposited energy is available. To refine the result the expected response of the calorimeter to these hypothetical hits is compared to the actual amplitudes in all cells.

The output of these procedures is a number of tracks of charged particles and calorimeter hits, which are written along with the fit errors to the output file. For tracks beginning in the first zone the starting point is assigned to the extrapolation of the track into the target plane ($z = 0$).

4.5 The analysis software

The purpose of the last program in the chain is to extract the relevant information from the abundant output of CORAL. The generated ROOT tree contains besides the participants in the original interaction also pileup particles and all other tracks generated by interaction of the beam with the detector.

For histogramming and display of the results ROOT was used. ROOT is a C++ library for data analysis in high energy physics developed in the context of the NA49 experiment at CERN. It is designed to deal with huge amounts of data in a way that specific parts of the objects can be accessed without reading all of the contents. This way it provides fast access to the interesting portion of data. Further information can be found on the web page [ROO].

Although the analysis steps were rather simple compared to the reconstruction this program had to be run in parallel. The total size of the ROOT trees of one run is about 3GB. Even if the the involved libraries would have been able to deal with files of this size, the time to read this data from disk would have been very long. For debugging the setup and trying new algorithms this software had to run often, so a computing time reduction by a factor of 64 was very welcome.

The analysis program consists of two parts: the master starts slave processes on each cluster machine which analyze the ROOT files whose names are transferred by the master. After processing one file the produced histograms are sent to the master which adds up the results and distributes new work.

To enable communication between the processes on different computers the PVM⁹ library [PVM] was used to spawn the slave jobs. This library permits efficient sending and receiving of messages over the network. As the ROOT library is written in C++, CPPvm¹⁰ [CPv]—a C++ wrapper for PVM—was used to write the parallelization code. CPPvm uses the concept of data streams common to C++ libraries [Str97] while ROOT objects provide a way to store their contents in a simple buffer. Within the scope of this thesis a class was written that permits the sending and receiving of ROOT objects through CPPvm streams utilizing the advantages of both approaches.

4.6 Testing the prerequisites

To test the simulation chain a series of tests were performed. The goal was to eliminate systematic reconstruction errors introduced by differences in the detector setup seen by COMgeant and by CORAL. Furthermore single particle events were used to measure the geometric acceptance of the spectrometer and its maximum momentum and angle resolution. Before starting the real simulation with Primakoff and Fritiof events also the influence of secondary interactions had to be examined.

⁹Parallel Virtual Machine

¹⁰C Plus Plus PVM

For comparison the terms *generated* and *reconstructed* will be used, the first denoting the input to COMgeant and the latter the output of CORAL.

To depict reconstruction errors and to quantify the corresponding resolution two types of plots will be used. In the first case two-dimensional plots will show the count rates. On the x axis will be the observable to be measured and on the y axis the deviation from the original value. When such a distribution is cut into slices parallel to the y axis, for each slice a mean value and a standard deviation (RMS¹¹) can be calculated. The mean value permits the detection of systematic shifts while the RMS is a measure for the resolution. This data will be plotted as a one-dimensional histogram called profile with the levels corresponding to the mean and the error bars corresponding to the RMS.

4.6.1 Tests with single π^- events

The setup was tested with events from the single particle generator described in section 4.2.1, containing only one primary particle—a pion with a momentum between 1–200 GeV and polar angles between 0–10 mrad. The distributions of these observables are shown in fig. 4.1 and fig. 4.2. The primary vertex is located at the exact center of the target. The target was a cylindrical Lead plate 4 cm in diameter with a width of 3 mm.

4.6.1.1 Interactions disabled

First the response of the detector was tested under ideal circumstances. Therefore all secondary interactions were switched off in COMgeant.

Fig. 4.1 shows the momentum and fig. 4.2 the angle distributions for the generated pions. The momentum components perpendicular to the beam axis are shown in fig. 4.3. They expose a clear peak at zero because of the flat θ distribution which is further enhanced by the small momenta present in the sample.

Without secondary interactions all pions of this sample with momentum greater than 3 GeV are successfully reconstructed. This implies that with the exception of very small energies all generated pions were in the acceptance of the spectrometer.

Since no other hits were generated in the detector the deviation from the original momentum is only due to the limited spatial resolution of the tracking stations.

¹¹Root Mean Square, $\sigma_x = \sqrt{\sum(x_i - \bar{x})^2}$

4 THE MONTE CARLO SETUP

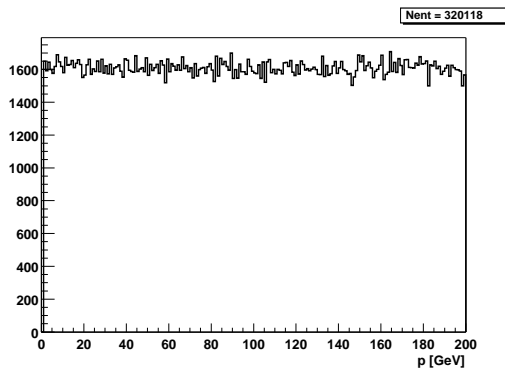


Figure 4.1: momentum distribution of the generated π^-

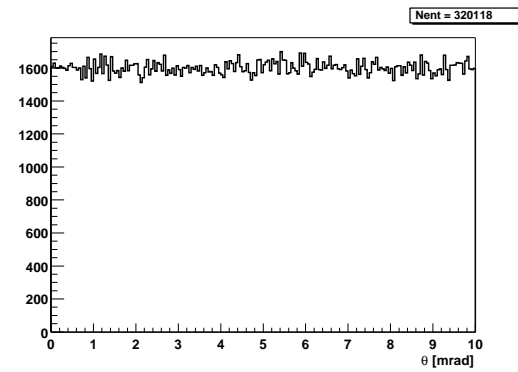
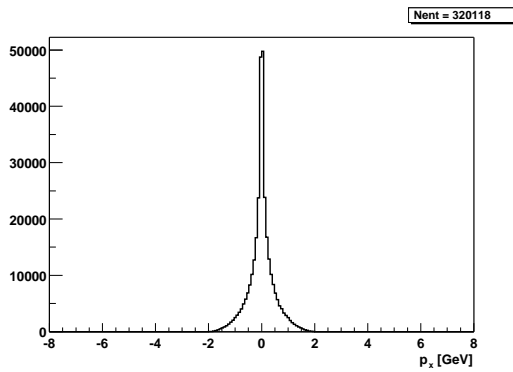
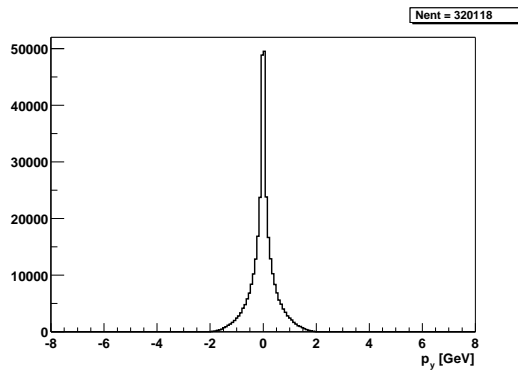


Figure 4.2: θ distribution of the generated π^-



(a)



(b)

Figure 4.3: x (a) and y (b) momentum components

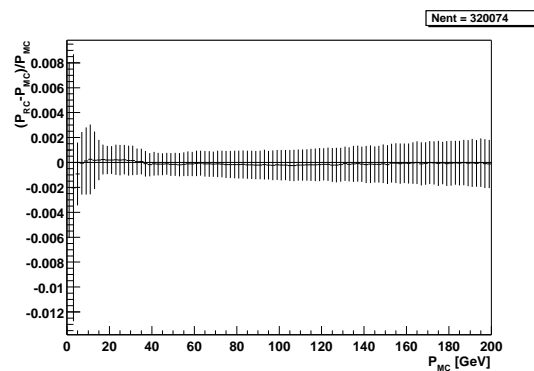
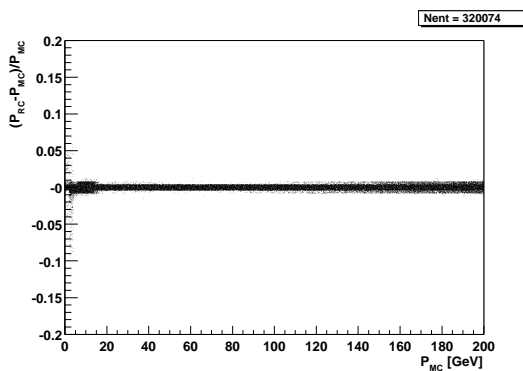


Figure 4.4: relative momentum reconstruction error and momentum resolution

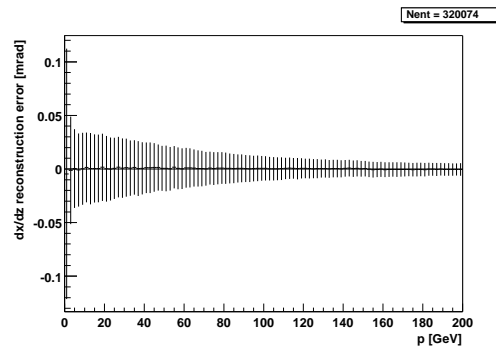


Figure 4.5: angular resolution vs. momentum

Because of the global fit during the last step of the track reconstruction, the resolution gets better with every tracking station that contributes to the track information. Thus, the higher the particle's momentum, the straighter is its trajectory and more hits are produced in the high resolution detectors near the beam axis. The big number of tracking detectors and the angular distribution of the pion momenta smear out the discrete steps of improving resolution. This effect produces the angular resolution shown in fig. 4.5. The x direction was more closely examined since the magnetic field of the spectrometer magnets is parallel to the y axis for small angles. Thus systematic errors would show up correlated in the total momentum and its x component.

The momentum resolution and its systematic reconstruction error are depicted in fig. 4.4. In this case the deflection of the particle by the magnetic fields of the spectrometer is used to determine its momentum. As shown in section 2.2.2 the deflection angle is anti-proportional to the momentum. Hence for constant angular resolution the relative momentum reconstruction error would be proportional to the momentum. This worsening of resolution for increasing momentum is lessened by the effect described in the context of the angular resolution.

To get such a clean plot with systematic momentum errors below 0.03% took long debugging of the setup. One example for a typical error was the description of the RICH. Because of the high beam intensity an Aluminum beam pipe filled with Helium was added. Otherwise the detector would be flooded with Cherenkov light from the beam particles. The medium description for the Helium chosen did not allow for a magnetic field inside this volume. Thus the fringe field of SM1 had a cylindrical hole resulting in less field seen by particles with high enough energy to pass through this area. This subtle effect of about 1% could only be seen because CORAL does not get information about the geometrical details but only about the active detector areas. So from the viewpoint of CORAL the field described in the field map covers everything including the beam pipe. The particle

4 THE MONTE CARLO SETUP

being less deflected by COMgeant gets reconstructed with a higher momentum in CORAL.

The intrinsic momentum resolution of the spectrometer is between 0.1% and 0.3% depending on the energy while the intrinsic angular resolution for a single direction is between 10–40 μrad depending on the energy.

4.6.1.2 All interactions enabled

To get as close as possible to real events single pions with the same characteristics were tracked with all interactions enabled. These are:

- decay in flight
- multiple scattering
- nuclear fission induced by a photon
- muon-nucleus interaction
- energy loss (Bethe-Bloch with fluctuations)
- photoelectric effect
- Compton scattering
- pair production
- bremsstrahlung
- Rayleigh effect
- delta ray production
- positron annihilation
- hadronic interaction
- light absorption
- synchrotron radiation

All particle tracking in COMgeant is subject to certain energy cuts. The internal default of 500 keV was used during all simulations. This means that energy losses of less than 500 keV are approximated by a continuous process. Also secondary

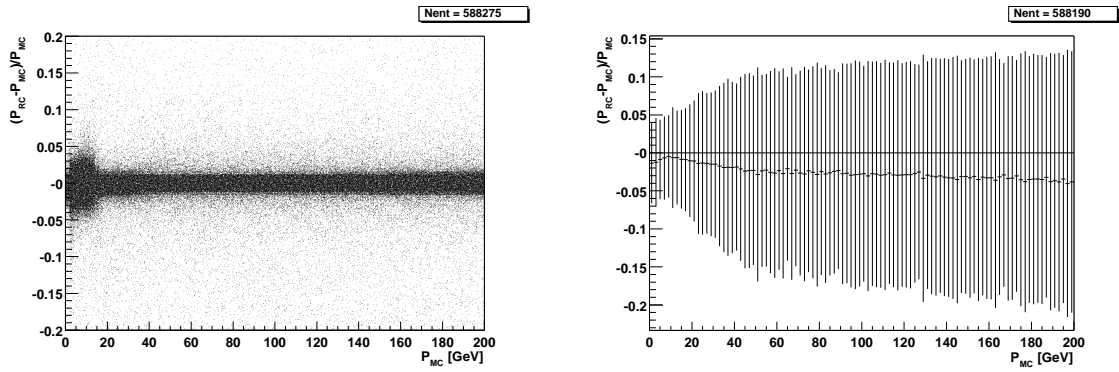


Figure 4.6: relative momentum reconstruction error

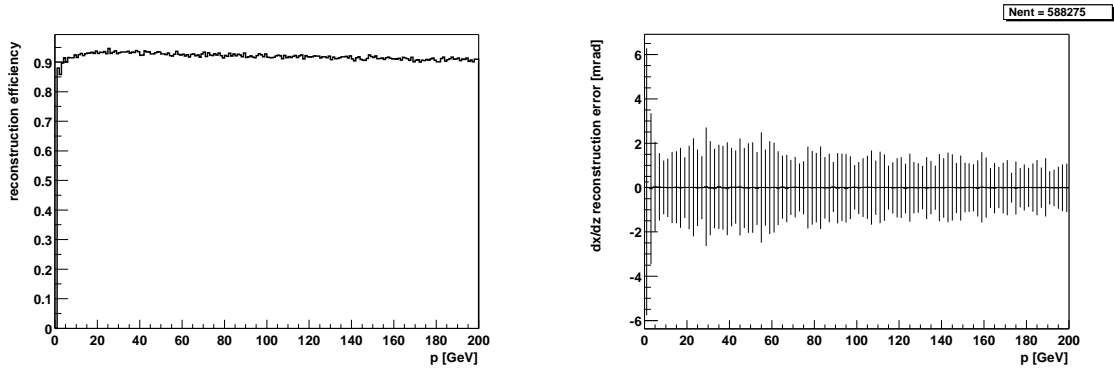


Figure 4.7: reconstruction efficiency with secondary interactions

Figure 4.8: angular resolution vs. momentum

particles produced with less than this energy are discarded and the development of the calorimeter showers stops at this granularity.

The number of tracks per event increases considerably due to the various processes so the selection of the right track raises issues. Since no other tagging was possible an event had to have exactly one track matching some criteria to count as reconstructed. The criteria applied were

- negative charge
- momentum between 0.2–250 GeV
- the track begins at the target position

The last condition does not imply a reconstructed vertex. It only means that the track is extrapolated to $z = 0$ what is always possible if it is seen in the first zone.

4 THE MONTE CARLO SETUP

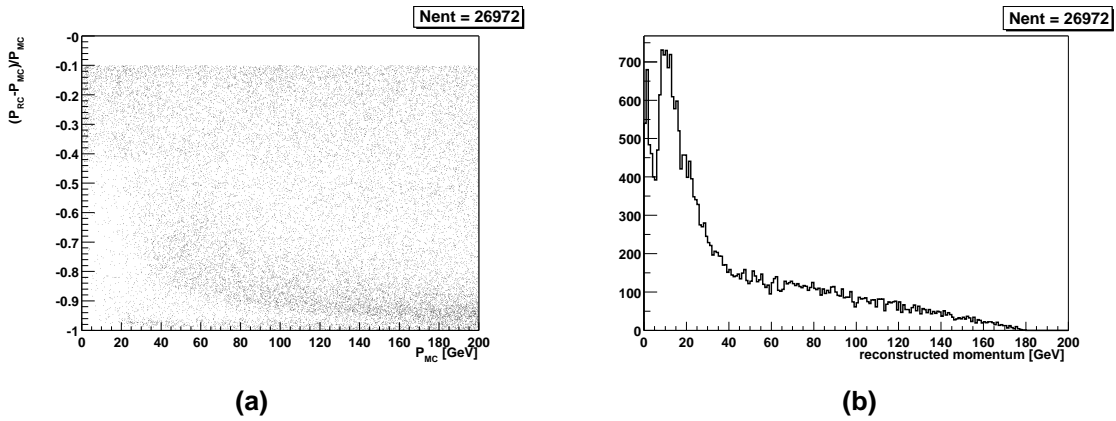


Figure 4.9: momentum reconstruction error (a) and reconstructed momentum distribution (b) for events with at least 10% relative momentum reconstruction error

Under these conditions the efficiency drops to about 92% (see fig. 4.7). While the momentum error scatter plot in fig. 4.6 looks good at first sight, the profile exhibits a systematic shift towards too low momenta of up to 3%. The reconstruction of the x direction does not show a shift, but the resolution of 1.5 mrad shown in fig. 4.8 is bigger than expected, as the effect of multiple scattering is proportional to p^{-1} and thus the angular resolution should approximate the case without interactions for high momenta.

The explanation of these effects lies in the physical processes that are simulated. Fig. 4.9a shows the distribution of all events that are more than 10% off with respect to the generated momentum. The area is completely filled but some structure is seen, especially when looking at the reconstructed momentum distribution of fig. 4.9b. The peaks at 1 GeV and 10 GeV are exactly the energies required to pass SM1 and SM2 respectively, what leads to the hypothesis that the particles produced by secondary interactions are falsely recognized as the searched-for pions. This hypothesis is examined more closely in the following.

The most common process is hadronic interaction of the π^- with a nucleus. Because of the structure of QCD many pions and other hadrons are produced in such reactions, preferably with low energies. The existence of two peaks originates in the two stage setup of the spectrometer: To be reconstructed a particle with less than 10 GeV has to be tracked through SM1 and thus needs to be produced before the magnet. For the same reason higher energy particles must be produced before SM2 to be falsely recognized. Since the distance from the target to SM2 is about five times bigger than the distance from the target to SM1 events of the latter type are more frequent by a factor of four. This enhances the numbers for energies above 10 GeV to produce a second peak.

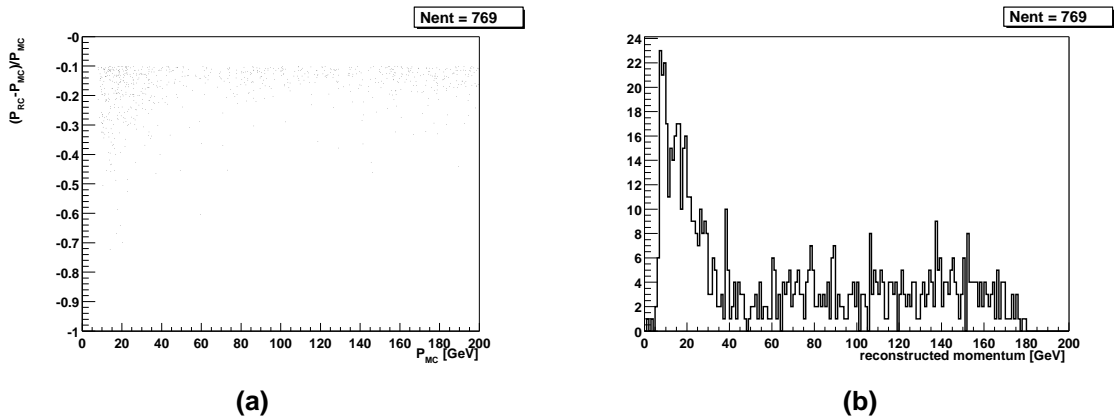


Figure 4.10: momentum reconstruction error (a) and reconstructed momentum distribution (b) for events with at least 10% relative momentum reconstruction error after applying the interaction cut

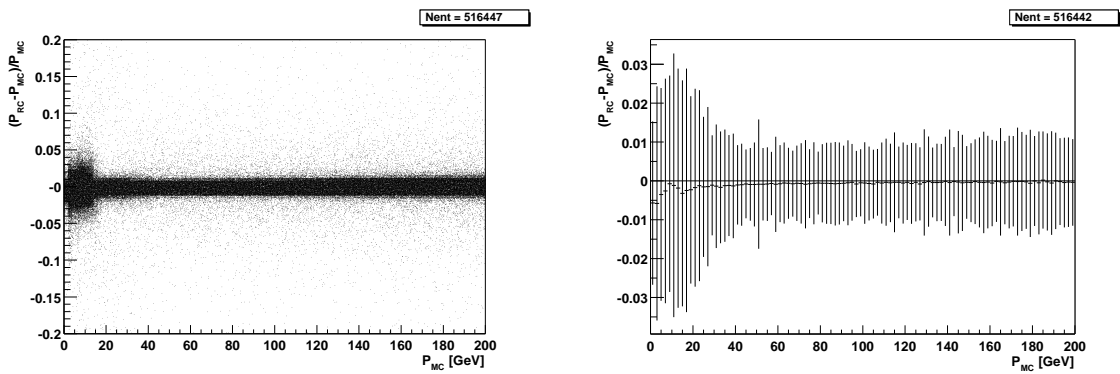


Figure 4.11: momentum reconstruction error

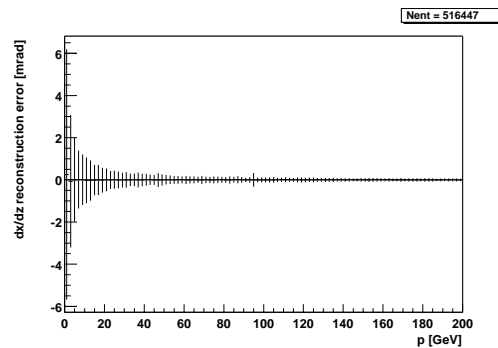


Figure 4.12: direction reconstruction error

4 THE MONTE CARLO SETUP

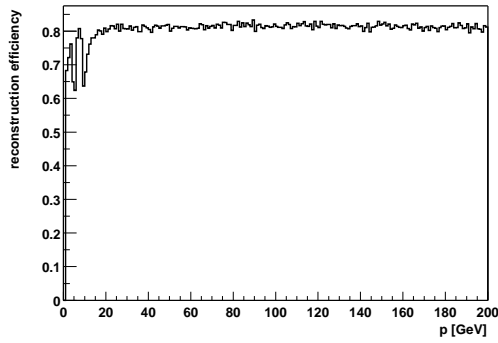


Figure 4.13: reconstruction efficiency

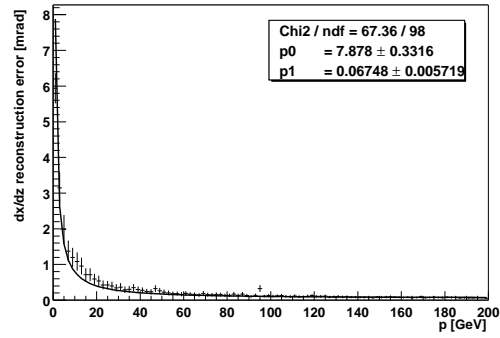


Figure 4.14: angular reconstruction error with fit parameters for multiple scattering and the intrinsic spectrometer resolution

To prove this explanation a further cut was imposed during the extraction of the information from the COMgeant particle lists. For a track to be accepted it was required that the original pion had not interacted before hitting a calorimeter or leaving the detector. The result is shown in fig. 4.10 –4.13. The number of events being more than 10% off decreased from 26972 to 769 while the efficiency dropped by the 15% that were filtered out.

At high energies the systematic momentum shift is gone. The reason for it partly persisting in the low energy case can be traced to the rather complex cut that was used to reject the pions that interacted before hitting a calorimeter or the yoke of a magnet. If all events are rejected where the pion did not leave the detector or reach the front of ECAL2 the reported efficiency drops to zero at energies below 5 GeV.

The angular resolution is mainly given by the momentum dependent multiple scattering and the intrinsic angular resolution of the spectrometer. Using a constant value for the latter, the momentum dependence should be

$$\Delta_{\frac{dx}{dz}} \approx \sqrt{\left(\frac{C_1}{p}\right)^2 + C_2^2} \quad (4.1)$$

A fit of this function to the angular resolution is shown in fig. 4.14 and gives a momentum dependence of

$$\Delta_{\frac{dx}{dz}} \approx \sqrt{\left(\frac{(7.88 \pm 0.33) \text{ mrad GeV}}{pc}\right)^2 + (67 \pm 6)^2 \mu\text{rad}^2} \quad (4.2)$$

The constant term for the intrinsic resolution is compatible with the resolution measured without interaction and shown in fig. 4.5. The description of multiple scattering given in [PDG00] is

$$\Delta_{\frac{dx}{dz}} \approx \frac{13.6 \text{ MeV}}{\beta c p} \sqrt{\frac{x}{X_0}} \quad (4.3)$$

As will be discussed later the target is 16% of the radiation length and produces a divergence of $\frac{5.5 \text{ mrad GeV}}{pc}$. Assuming that only the first half of the spectrometer has a significant influence on the direction reconstruction, the multiple scattering in this region has to be added. The first 10 m of the detector add up to 25% radiation length, corresponding to an accumulated divergence of $\frac{6.8 \text{ mrad GeV}}{pc}$. The total effect of these two contributions is $\frac{8.7 \text{ mrad GeV}}{pc}$. This makes plausible that the loss in angular resolution for small momenta is due to multiple scattering.

The feature to notice in fig. 4.11 is the decrease in resolution below 35 GeV. This is caused by the space reserved for RICH2 in the setup, as pions produced in forward direction only hit the tracking station upstream of ECAL2 if their energy is above 30 GeV. If the sample would only contain particles produced along the z axis there would be a sharp change in resolution at this threshold because of the big change in lever arm, but since the sample contains angles up to 10 mrad this edge is smeared out.

4.6.2 Tests with single γ events

In addition to the tracking of the pion the detection of the produced photon is vital to the analysis of Primakoff scattering. Therefore another test was conducted with single photon events. Concerning the direction and energy the same settings were used as for the single pion events. To test only the calorimeter all following plots except the conversion point plot are calculated only for events where the photon did not convert before hitting the calorimeter.

Fig. 4.15 shows the energy range and the directions covered by the sample after the conversion cut. The fact that the energy distribution remains flat after the cut confirms that the conversion cross section is constant over this energy range. The sharp peak in the center of the direction distribution is again due to the flat θ distribution.

Of the 640000 generated photons about 271000 converted upstream of the back side of SM2. With the current status of the reconstruction software the e^+e^- -pair cannot be recombined to give the conversion vertex, so the measurement can only be successful if the photon does not convert or the e^+e^- -pair does not traverse a

4 THE MONTE CARLO SETUP

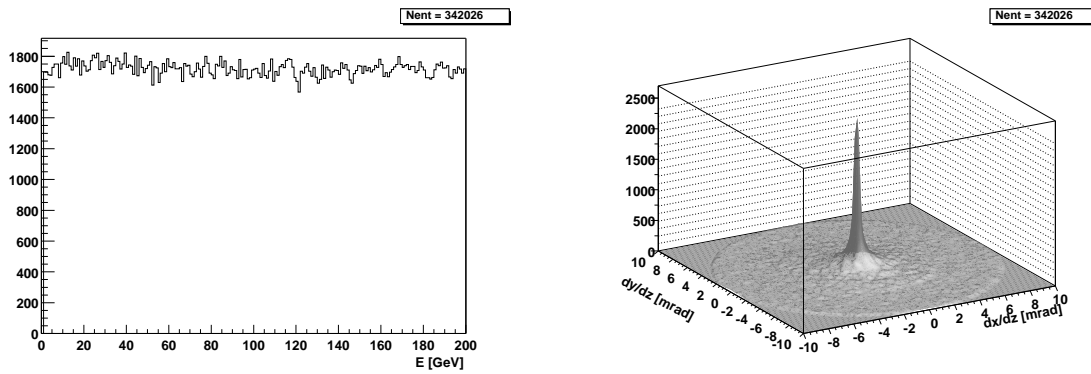


Figure 4.15: energy and direction of the generated photons

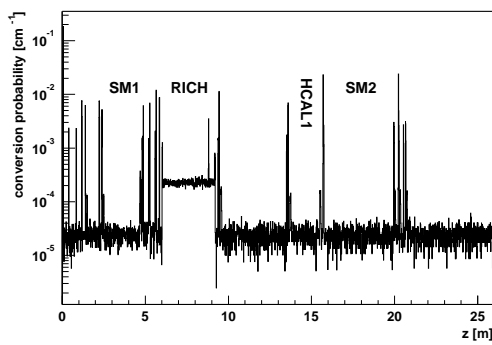


Figure 4.16: z-coordinate of conversion vertex

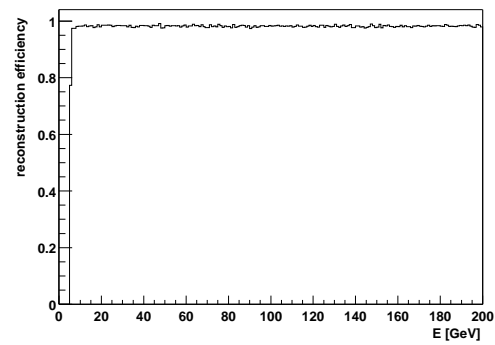


Figure 4.17: reconstruction efficiency

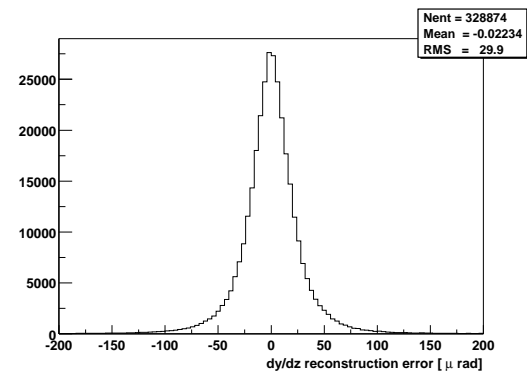
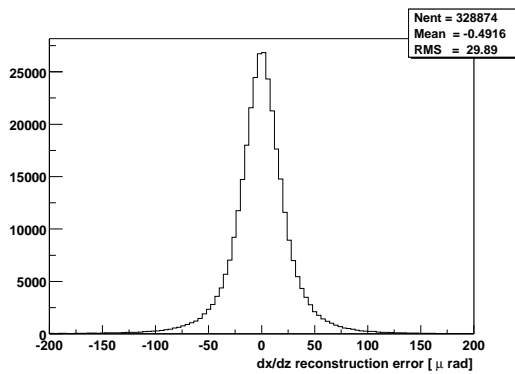


Figure 4.18: direction reconstruction error

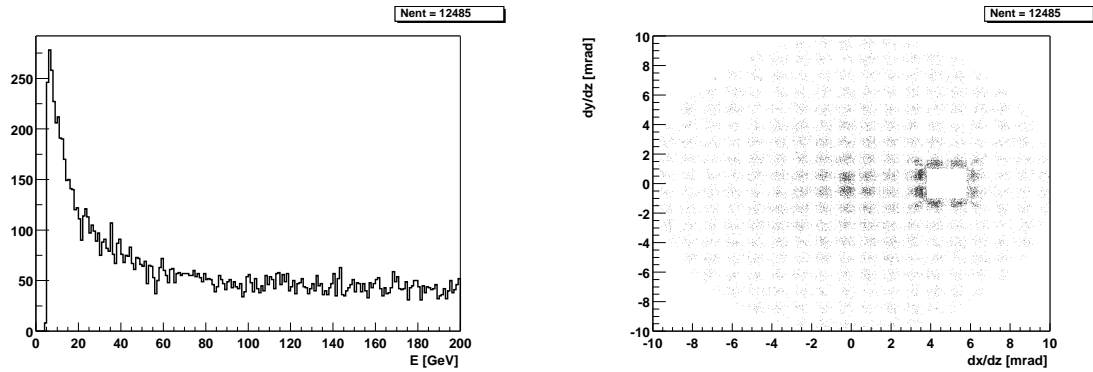


Figure 4.19: photon energy and direction for events with big position reconstruction errors

magnetic field before hitting the ECAL. In the latter case all energy will still be collected in the same calorimeter shower since the maximum angle the leptons can have in the case of a 100 GeV photon is of the order of 1 mrad. The distribution of the position of the conversion vertex is shown in fig. 4.16. The contents of each bin is normalized to the photon flux entering this section of the spectrometer, so it depicts the local conversion probability. All detector stations can clearly be seen as peaks above the background of conversions in mid air. Also very prominent is the RICH because of its gas filling of C_4F_{10} . Although not very prominent in the plot, it has to be noted that the conversion probability is 19% inside the target.

To select the hit in the ECAL2 from the particles presented by CORAL a simple threshold approach was used. The hit with the highest energy deposition was selected if it contained more than 5 GeV. This results in total inefficiency below 5 GeV as can be seen in fig. 4.17. The reason for this cut is to avoid misleading hits in case the real photon is out of the acceptance of the calorimeter. Besides, the low energy photons will not be interesting for the analysis presented in the next chapter. Above 5 GeV the efficiency is constantly around 98%. The loss of 2% is due to the physical hole of the calorimeter that can be seen in the right plot of fig. 4.19.

The spatial resolution of the calorimeter translates directly into the angular resolution on the photon direction which is shown in fig. 4.18. The average angular resolution of $30 \mu\text{rad}$ denotes a spatial resolution of 1.0 mm. The distribution shown has longer tails than a Gaussian function. This is caused by the superposition of different photon energies onto one plot. Fig. 4.19 shows the energy and direction distributions for events with a direction reconstruction error greater than $50 \mu\text{rad}$.

First, more events with low energy are affected. These photons correspond to the

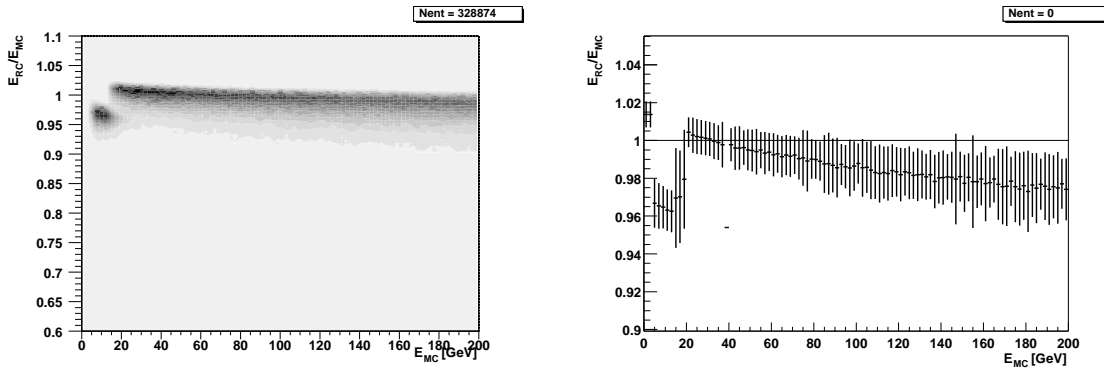


Figure 4.20: energy reconstruction error and resolution

entries in the direction distribution which are evenly scattered across all calorimeter cells. A low energetic photon will produce a small shower in the calorimeter. If this happens near the center of one cell only a very small fraction of the energy is collected in neighboring cells. This leads to a bad spatial resolution. The grid that is visible in the figure corresponds to the cell structure of the calorimeter, the white lines lying on the cell boundaries.

The second thing is the big number of entries near the hole of the calorimeter. For hits in the cells adjacent to the hole, part of the energy is lost so position and energy reconstruction suffer. This effect increases with energy because of the broadening shower and creates the long tail seen in the energy spectrum.

Fig. 4.20 shows the energy reconstruction error. The profile exhibits a systematic shift towards too small values which is increasing with incident photon energy. For 200 GeV photons the reconstructed energy is about 4% off while the resolution is 3%. This resolution was obtained by fitting a Gaussian function to the distribution in each energy bin. However, the profile does not reflect the long tail that the distribution has, ranging down to 0.5 for big energies. Even though the ECAL2 has about 20 radiation lengths, a substantial part of the shower can reach its end and is not measured by this calorimeter.

HCAL2 is positioned directly after ECAL2. Therefore the shower remnants which exit the ECAL will hit the HCAL, as shown in fig. 4.21. This diagram depicts the position of energy deposition in the HCAL relative to the extrapolated photon hit. It exhibits a clear peak at the expected position with a width of 5 cm. It is straight forward to collect the energy found in this region of the HCAL2 and add it to the energy reconstructed in the ECAL. Fig. 4.22 shows the relation between these two energies. The cut at 0.7 GeV on the y -axis originates from the threshold for HCAL reconstruction.

Applying this correction gives a reconstructed energy which is about 1% too high,

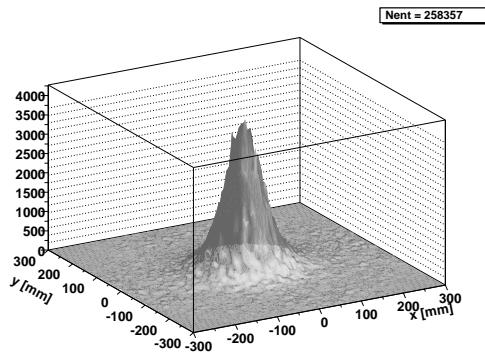


Figure 4.21: position of the energy deposition in the HCAL2 relative to the extrapolated photon hit

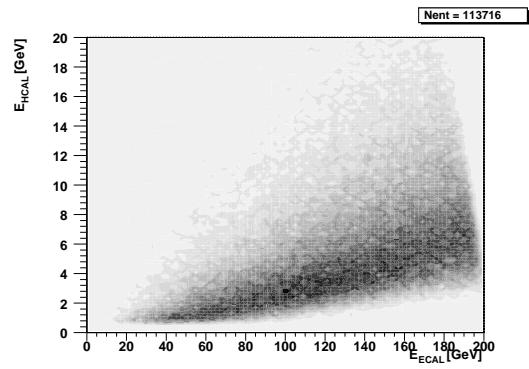


Figure 4.22: energy found in HCAL2 near extrapolated photon hit vs. energy in ECAL2 hit

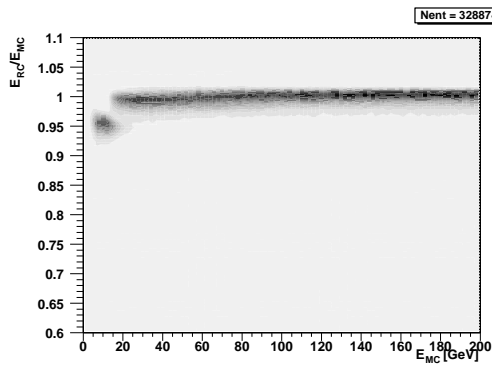
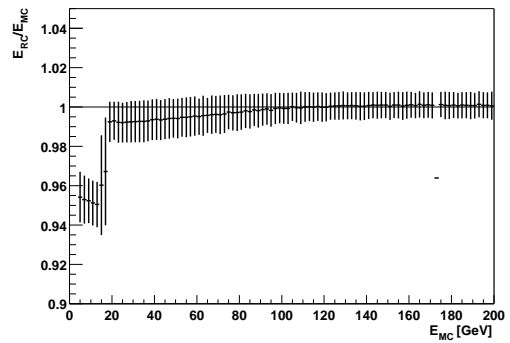


Figure 4.23: energy reconstruction error and resolution after the leakage correction



probably due to the calibration of the HCAL which is not tuned for low energy photon hits, so a factor of 0.987 was applied to the obtained value. The result is shown in fig. 4.23. It has two features: the obvious problem at energies below 15 GeV persists, so this has a different origin. Second, below 100 GeV the correction does not work completely, failing worse for lower energies. This is because in this case the energy in the HCAL only amounts to some 100 MeV, which is below the HCAL reconstruction threshold. However, for the intended simulation photon energies below 90 GeV will not be of interest.

Although the longitudinal leakage explains the systematic shift the correction cannot be used in the real experiment. The noise of the real HCAL2 is too big to search for a 1 GeV hit that happens only a few cells apart from the much bigger hit of the scattered pion or beam particles. A possible solution would be to use a Lead plate to start the shower earlier and reduce the chance for particle escape. As this increases the threshold for particle detection it is limited by the cut on the photon energy in the Primakoff trigger which will be of the order of 50–60 GeV. How seriously the energy resolution would be affected by this measure remains to be studied.

4.6.3 Test summary

The relative momentum resolution for π^- with all interactions accounted for is 1% for energies above 35 GeV and up to 2.5% below this mark. The angular resolution in a single coordinate is $\frac{10.5 \text{ mrad GeV}}{p}$.

The position resolution for the photon in the calorimeter is 1.0 mm corresponding to an angular resolution of 30 μrad . In the interesting energy range the energy resolution is better than 1% after taking into account the leakage into the HCAL.

All generated pions with energy greater than 2 GeV were in the acceptance of the spectrometer, the reconstruction efficiency with interactions enabled is 92%. The photon acceptance is 98% due to the beam hole of ECAL2 while the reconstruction efficiency is only 58% as a result of pair production within the spectrometer.

In the more specific investigation of Primakoff Compton scattering the characteristics of this reaction have to be taken into account. The angular distribution of the produced photons is more focused in the forward direction so that the acceptance cut introduced by the beam hole of the ECAL2 is nearly negligible.

Chapter 5

Simulation

This chapter describes the results of the simulation of Primakoff Compton scattering. After an introduction to the run conditions in section 5.1, the event selection and reconstruction methods are described in section 5.2. In section 5.3 rate estimates are given, followed by the retrieval of the polarizability parameters in section 5.4. Here the same naming convention as in section 4.6 will be used: *generated* stands for the input to COMgeant while *reconstructed* denotes the output of CORAL. The chapter ends with remarks on the strength of the expected hadronic background and the influence of systematic reconstruction errors.

5.1 The run conditions

In contrast to the single particle tests presented in the previous chapter there are many particles in each Primakoff event. First there always is the beam particle that is stored in a special way: its three-momentum is inverted so it moves upstream from the target. Then there is the scattered pion and the produced photon, both moving downstream. These three particles emerge from the primary vertex whose position is randomized inside the target.

In COMgeant these particles are tracked through the spectrometer as described in section 4.3, producing secondary particles as they interact with the detector material. As these are also tracked they also produce hits in the detectors and have to be reconstructed.

The most frequent interactions are hadronic interactions with heavy nuclei for the pions and conversion for the photons. As these interactions heavily change the tracks that the particles leave in the detector they can be easily identified. Another complication is the fact that each trigger opens a window of 80 ns in

5 SIMULATION

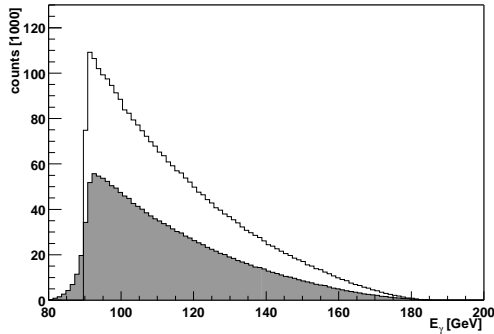


Figure 5.1: generated (white) and re-constructed (shaded) photon energy in the laboratory frame. The data of all five samples is merged ($2.9 \cdot 10^6$ events)

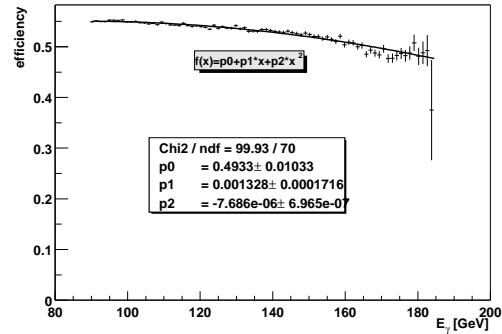


Figure 5.2: reconstruction efficiency vs. photon energy in the laboratory frame. The error bars are the binomial errors corresponding to the generated statistics shown in the left hand plot

the readout. During this time non-interacting beam particles will traverse the detector because of the high beam intensity. The hits produced by these particles are called pileup and lead to further tracks in the reconstruction. If too many of these hits are close to the tracks of the original interaction the reconstruction can fail. This effect reduces the overall efficiency for tracks that are close to the beam. Since the latter condition implies a high particle momentum the selected Primakoff events with pion momenta below 100 GeV are less affected.

To study the influence of the polarizabilities on the reconstruction, five samples with different values for the parameters are produced, each with a statistics of 620.000 events.

5.2 The reconstruction method

The following cuts are used to recognize Primakoff events: there has to be a photon hit in the ECAL above a certain energy and a negative charged track which carries the complementary energy. The cut on the photon energy has to be well above the energy deposition of hadrons in the electromagnetic calorimeter that is of the order of some GeV. In order to select the so-called “hard events” with most information on the pion polarizabilities, this cut is raised to 30–50% of the beam energy. In this simulation a cut on the photon energy at 90 GeV was implemented in the generator, so it was natural to use 80 GeV in the reconstruction. The energy window for the sum of pion and photon was set to 180–196 GeV to allow for the longitudinal energy leakage of ECAL2.

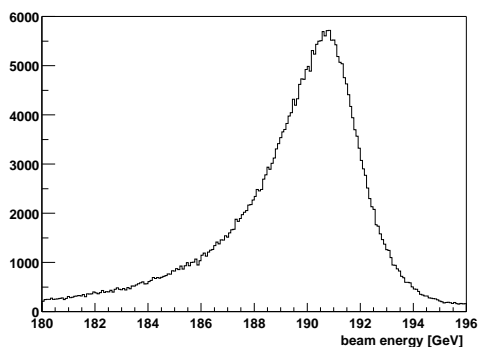


Figure 5.3: reconstructed beam energy

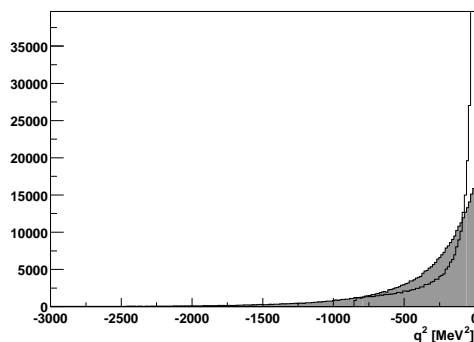


Figure 5.4: generated (white) and reconstructed (shaded) q^2

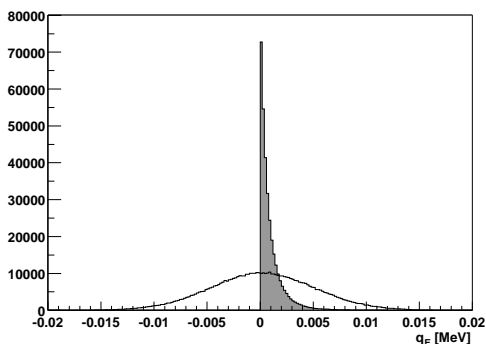


Figure 5.5: generated (white) and reconstructed (shaded) energy transfer in the laboratory frame

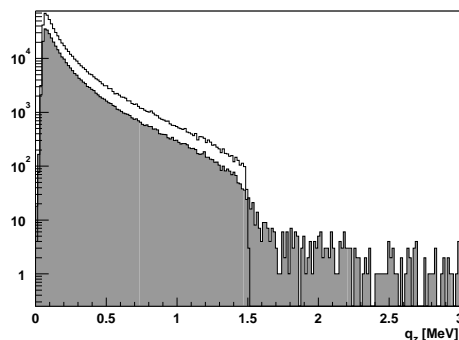


Figure 5.6: generated (white) and reconstructed (shaded) q_z

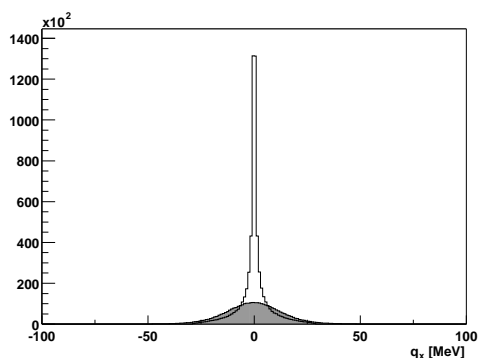


Figure 5.7: generated (white) and reconstructed (shaded) q_x

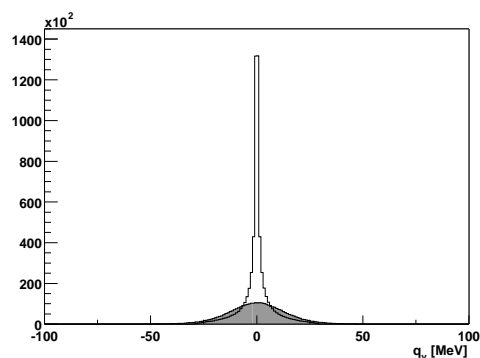


Figure 5.8: generated (white) and reconstructed (shaded) q_y

5 SIMULATION

The reconstructed count rates have to be corrected for the inefficiency of the detector before fitting the cross section. Since the overall effect of the polarizabilities is small, the generated photon energy distributions differ only slightly for different parameter values. Thus, to gather more statistics, the data of all five samples is merged to calculate the dependence of the reconstruction efficiency on the photon energy in the laboratory frame. Fig. 5.1 shows the generated and—with the cuts applied—the reconstructed photon energy in the laboratory frame, fig. 5.2 shows the corresponding efficiency with fit parameters. As expected from single photon and pion efficiencies the overall efficiency is between 50-55%.

The following figures were all produced only with the events that were left after applying the two cuts. At this stage the momenta of the outgoing pion and photon were available, but there was not yet a possibility to reconstruct the beam particle. In the generator the beam particle always has a momentum of 190 GeV along the z axis. The whole event is then rotated by the converter mentioned in section 4.2.2 to simulate a beam divergence of $0.3 \times 0.6 \text{ mrad}^2$. Instead of just using this beam momentum another approach was used for two reasons: in the experiment the beam energy will also be difficult to obtain directly and since the recoil of the nucleus is not measured the momentum transfer cannot be calculated this way.

The missing information on the beam energy is replaced by the assumption that the nucleus scattered elastically, expressed in the dispersion relation (3.1). This assumption is justified by the target recoil veto as explained in section 2.2.4 that will be installed for the measurement but could not be included in this simulation. Using the direction of the beam particle the following equation has to be solved:

$$f(P) = E + \frac{(\mathbf{P} - \mathbf{p})^2}{2M} - \sqrt{m^2 + P^2} \stackrel{!}{=} 0 \quad (5.1)$$

Here \mathbf{P} denotes the beam momentum, \mathbf{p} and E the total momentum and energy of the final state, m the pion mass and M the mass of the nucleus. Since the exact symbolic solution is too complicated to put into a program the Newton algorithm was used to solve it numerically:

$$P_{n+1} = P_n - \frac{f(P_n)}{f'(P_n)} \quad P_0 = p \quad (5.2)$$

The curvature of $f(P)$ is very small in the vicinity of the null and the correction to $P \approx p$ is small, so three iterations are sufficient to reach double floating point precision.

The consequence of this algorithm is that the calculated energy transfer will always be positive, as will be the z component of the momentum transfer. As the

dispersion relation is always obeyed the squared four-momentum transfer will be negative. This would not be the case if the whole beam momentum would be taken from the generator. In this case the peak at $q^2 = 0$ would be very much broader—as the q_z distribution would have a width of some GeV—and would also have a tail towards positive values because the reconstructed energy of the final state would not match the energy in the initial state. This would make it impossible to select small q^2 events.

The resulting beam energy and momentum transfer are shown in fig. 5.3–5.8. The symmetric distribution of the generated energy transfer is due to rounding errors: while the reconstructed momenta are calculated using double precision, the generated momenta are delivered only in single precision, so the energy resolution for the incident pion is about 2 keV. The quantization that would occur if the momenta were directly subtracted is smeared out during the calculation of the corresponding energies.

While the generated q^2 distribution exhibits a clear q^{-4} behavior the reconstructed q^2 is smeared out and behaves like e^{q^2} . This follows from the different information available on the three momentum components: the reconstructed q_z is very good, but the reconstructed transverse momentum transfer shows a much broader distribution than the generated one. An estimate of the transverse momentum transfer error induced by angle reconstruction errors of the final state can be made from the resolution tests in section 4.6.1 and section 4.6.2. Quadratically adding the errors for 110 GeV photon energy and 80 GeV pion momentum yields an error of 15 MeV. This is in good agreement with the width of the shaded area in fig. 5.7 and fig. 5.8.

Since this error in the reconstruction of the transverse momentum transfer can only increase the value for q^2 it flattens the pole at $q^2 = 0$. Nevertheless the rise is steep enough to permit a cut at $-q^2 < 1000 \text{ MeV}^2$. Such a cut reduces the efficiency by 6%, but it characteristically changes the count rates in each bin of the cross section. As the correction has not yet been determined this cut was only used to obtain a preliminary estimate of the hadronic background that is presented in section 5.5; the count rates and fits shown in section 5.4 were obtained without this cut. Further study of the properties of this cut is necessary to correctly estimate the systematic errors it introduces.

5.3 Rate estimates

According to its screen output the cross section simulated by Polaris is 12.6 mbarn. The cut on the photon energy at 90 GeV reduces this by a factor

5 SIMULATION

of 25, so the integrated cross section for the simulated process is 0.5 mbarn. The particle density of a 3 mm Lead plate is $9.9 \cdot 10^{21} \text{ cm}^{-2}$ yielding an interaction probability of $5 \cdot 10^{-6}$, so the simulated statistics of 620.000 correspond to a flux of $1.24 \cdot 10^{11}$ pions.

The expected flux for the hadron beam is $2 \cdot 10^7 \text{ sec}^{-1}$ while the spill structure provides 5 sec beam every 16 sec. With an assumed combined efficiency of COMPASS and the SPS of 60% [Olc01] $3.2 \cdot 10^{11}$ pions per day are expected.

5.4 Retrieving the polarizabilities

As described in section 3.2.2 the generated and reconstructed four-momenta are transformed to the projectile frame¹. As already shown there, the cut on the photon energy in the laboratory frame shows up as a cut in the energy/angle plane as depicted in fig. 3.4 on page 22. All bins that are affected by that cut are not used in the fit of the cross section and are therefore emptied in the histograms.

The fit is performed using the ROOT interface to the MINUIT [MIN] package. The function to be fitted is the interaction rate multiplied by a certain time so that the number of interactions is equal to the number of simulated events. The interaction rate is given by the product of the cross section (3.34) and the luminosity, that in turn is the product of the beam particle rate and the area density of atoms in the target. Since the external measurement of the luminosity could possibly be inaccurate the factor of measurement time and luminosity was one of the fit parameters. From now on it will be called the flux factor ϕ . Instead of the intended cut at $-q^2 < 1000 \text{ MeV}^2$ the Polaris configuration file contained a setting of $-q_{\text{max}}^2 = 850 \text{ MeV}^2$. As this was discovered after the completion of the time consuming simulation and the difference is not big it was decided to continue with this cut. With a beam energy of $P = 190 \text{ GeV}$, the π^- mass $m = 139.57018 \text{ MeV}$ and $-q_{\text{max}}^2 = 850 \text{ MeV}^2$ the fit function is

$$f(\omega, \cos \theta) = \phi \frac{\alpha^2 Z^2}{m} \left(\ln \frac{575.938 \text{ GeV}^2}{\omega^2} + \frac{\omega^2}{1565.56 \text{ GeV}^2} \right) \cdot \left\{ \frac{\alpha}{m\omega} \frac{1 + \cos^2 \theta}{\left[1 + \frac{\omega}{m}(1 - \cos \theta)\right]^2} - 2\omega \frac{\bar{\alpha}(1 + \cos^2 \theta) + 2\bar{\beta} \cos \theta}{\left[1 + \frac{\omega}{m}(1 - \cos \theta)\right]^3} \right\} \quad (5.3)$$

The generated event rates and the corresponding fit parameters for the cross section simulated with $\bar{\alpha} = 3 \cdot 10^{-4} \text{ fm}^3$ and $\bar{\beta} = -2 \cdot 10^{-4} \text{ fm}^3$ are shown in fig. 5.9. The flux factor is given in multiples of 10^6 m^{-2} while the polarizability

¹outgoing π^- at rest

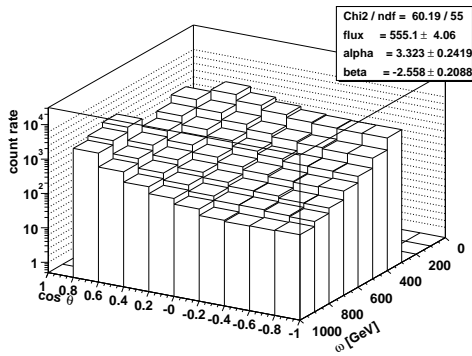


Figure 5.9: generated count rates with fit parameters

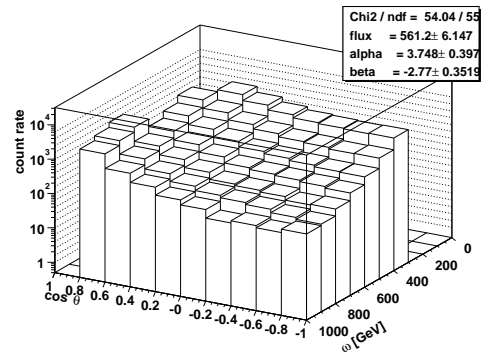


Figure 5.10: reconstructed and efficiency corrected cross section with fit parameters

parameters are given in the usual units of 10^{-4} fm^3 . The recovered polarizabilities $\bar{\alpha}$ and $\bar{\beta}$ differ from the ones fed into the event generator by $0.3 \cdot 10^{-4} \text{ fm}^3$ and $0.6 \cdot 10^{-4} \text{ fm}^3$ respectively. The reason for this discrepancy has not yet been found, however the comparison between the generated and reconstructed count rates can be investigated at this level.

To get the reconstructed differential cross section the event rates had to be corrected for the inefficiency of the detector. Eq. (3.18) was used to calculate the photon energy in the laboratory frame corresponding to each bin center. The fitted polynomial obtained in section 5.2 (cf. fig. 5.2) was then evaluated at this energy to calculate the efficiency for that bin. The bin content was divided by that efficiency to approximate the event rate for a detector with efficiency one. The uncertainty of this correction for high photon energies in the laboratory reference frame results in increased uncertainties of the corrected count rates in the region of great ω and $\cos \theta \approx -1$. While the reduced statistics account for a factor of 1.4 to the errors this local effect considerably increases the uncertainty of the polarizabilities.

The corrected event rates together with the fit parameters are shown in fig. 5.10. The errors given are the errors calculated by MINUIT, so they contain the statistical errors and the uncertainty of the efficiency correction. The distance in parameter space of the polarizabilities and flux factor found from the two fits is depicted in the correlation contour plots in fig. 5.12 and fig. 5.11. These plots show the shape of the χ^2 merit function in the vicinity of the minimum with respect to two fit parameters. The shapes are very elliptic, so the two parameters are highly correlated: in the left plot one could increase $\bar{\alpha}$ a bit while decreasing $\bar{\beta}$ by the same amount and the fit would not lose much quality. If both parameters are increased, the first boundary—signifying one standard deviation—is reached

5 SIMULATION

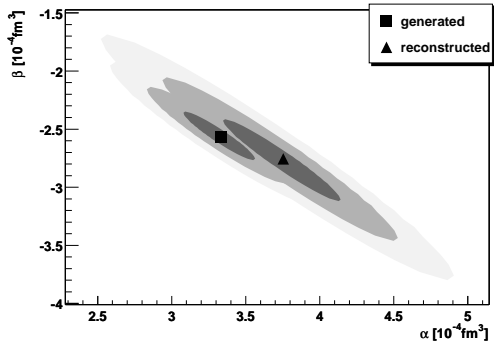


Figure 5.11: correlation contours of 1σ , 2σ and 3σ between $\bar{\alpha}$ and $\bar{\beta}$ for the generated and the reconstructed cross section

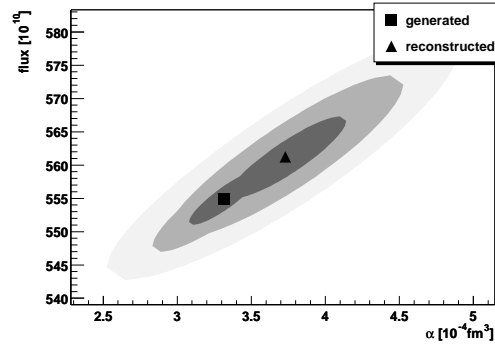


Figure 5.12: correlation contours of 1σ , 2σ and 3σ between the flux factor and $\bar{\alpha}$.

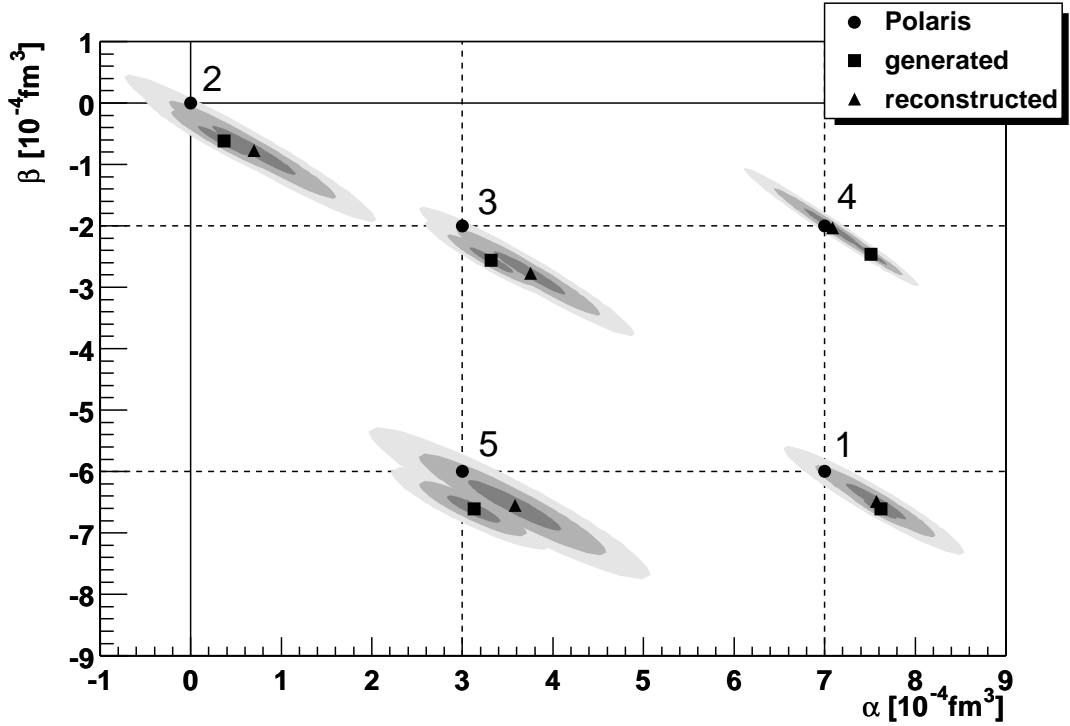
much earlier.

The fact that $\bar{\alpha}$ and $\bar{\beta}$ are anti-correlated means that $\bar{\alpha} + \bar{\beta}$ is determined with a much smaller error than $\bar{\alpha} - \bar{\beta}$. As discussed in section 3.4 the polarizability effect is proportional to $\bar{\alpha} + \bar{\beta}$ for $\cos \theta = 1$ and $\bar{\alpha} - \bar{\beta}$ for $\cos \theta = -1$, increasing with the photon energy like ω^2 . So $\bar{\alpha} - \bar{\beta}$ is mostly determined in the region with least events while $\bar{\alpha} + \bar{\beta}$ is better known because the cross section has a steep rise towards positive $\cos \theta$.

In contrast to the anti-correlation of $\bar{\alpha}$ and $\bar{\beta}$, $\bar{\alpha}$ and ϕ are correlated with a positive coefficient. This can be understood by considering the cut on the photon energy and the energy dependence of the polarizability effect. The region where the polarizability does not contribute to the cross section is unavailable to the fit because of the photon detection threshold that was set to 80 GeV in the reconstruction and 90 GeV in Polaris. Since a greater value of $\bar{\alpha}$ results in a smaller cross section this can be compensated in part by a higher flux factor.

As stated above the simulation was performed for five different polarizability pairs. The resulting fit parameters and confidence intervals are shown in fig. 5.13 together with the values for $\bar{\alpha}$ and $\bar{\beta}$ that were passed to the generator. All errors given in the table have been extracted directly from the MINUIT error matrix and give the 68.3% confidence interval (one standard deviation). The overall efficiency was 54% for all samples. The statistics of the fifth sample is 25% smaller due to a failure of the air conditioning for the computer cluster that prematurely ended the COMgeant execution.

Taking into account that the simulated statistics corresponds to ten hours of COMPASS data taking, the errors are promising. The five samples comprise the region of predictions and previous measurements summarized in section 3.7; the



	$(\bar{\alpha}, \bar{\beta})$	statistics	$(\bar{\alpha}, \bar{\beta})$		$(\bar{\alpha} + \bar{\beta}, \bar{\alpha} - \bar{\beta})$	
			generated (error)	reconstructed (error)	generated (error)	reconstructed (error)
1	7,-6	335620	7.62,-6.61 (0.18, 0.16)	7.57,-6.49 (0.33, 0.29)	1.01,14.23 (0.07, 0.33)	1.08,14.06 (0.10, 0.62)
2	0, 0	330950	0.37,-0.62 (0.29, 0.24)	0.70,-0.77 (0.46, 0.40)	-0.25, 0.99 (0.09, 0.53)	-0.07, 1.47 (0.13, 0.86)
3	3,-2	336128	3.32,-2.56 (0.24, 0.21)	3.75,-2.77 (0.40, 0.35)	0.76, 5.88 (0.08, 0.44)	0.98, 6.52 (0.11, 0.74)
4	7,-2	333545	7.51,-2.46 (0.18, 0.18)	7.09,-2.03 (0.32, 0.32)	5.05, 9.97 (0.04, 0.36)	5.06, 9.12 (0.05, 0.63)
5	3,-6	252072	3.13,-6.61 (0.30, 0.22)	3.58,-6.55 (0.52, 0.41)	-3.48, 9.74 (0.14, 0.51)	-2.97,10.13 (0.19, 0.92)

Figure 5.13: summary of the five simulated polarizability pairs. The circles give the values set in the generator configuration file, the squares the fit parameters obtained from the generator output and the triangles show the reconstructed polarizabilities. As in fig. 5.11 the contours show the 1σ , 2σ and 3σ confidence intervals. Only statistical errors are given in the table.

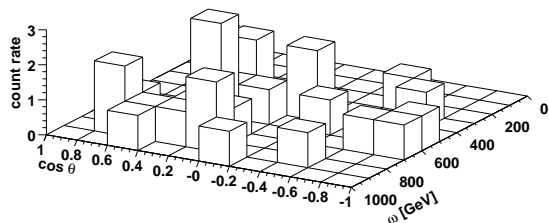


Figure 5.14: distribution of the accepted background events in the projectile frame. The generated sample contains $4.5 \cdot 10^6$ events.

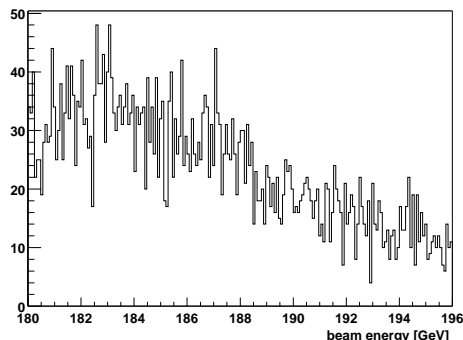


Figure 5.15: reconstructed beam energy for background events. This does only include the energy carried by the pion and the photon.

worst errors are obtained in the case of an unpolarizable pion, but still they are much smaller than the uncertainties quoted for the Serpukhov experiment and comparable to those of the theoretical predictions. Assuming 6% decrease in efficiency due to the q^2 cut and another 20% because of other cuts to reject background it would take one COMPASS day to collect an equivalent amount of data. Thus, one month of data taking would result in statistical uncertainties smaller by a factor 5.6: about 0.07 for $\bar{\alpha}$ and $\bar{\beta}$, 0.02 for $\bar{\alpha} + \bar{\beta}$ and 0.14 for $\bar{\alpha} - \bar{\beta}$.

In addition to the statistical errors a systematic shift is seen between the initial parameters and their fitted values both for the generated and the reconstructed polarizabilities. As the momenta delivered by Polaris directly are passed through COMgeant and CORAL and only undergo one Lorentz boost before they are histogrammed and fitted, the reason for the significant deviation between the input to and output from Polaris has not yet been found. This discrepancy requires further study to enable the interpretation of a future measurement. For the reconstructed data the deviation is not in all cases significant, but the shift direction is the same for all five samples: while $\bar{\alpha} + \bar{\beta}$ neatly matches the initial value the reconstructed $\bar{\alpha} - \bar{\beta}$ is too big in all cases. It is likely that both deviations result from one problem that remains to be isolated.

5.5 Strength of hadronic background

To investigate the corruption of the measured Primakoff cross section by hadronic background events, a large sample of minimum bias events was produced with the Fritiof generator introduced in section 4.2.3. The analysis of 4.500.000 events

by the exact process described above accepts only 34 events, 27 of them were in the fit range for the polarizabilities and are shown in fig. 5.14.

As Fritiof only simulates hadronic interaction the mechanism for accepting some of the events is the production of π^0 or η . According to [PDG00] the η decays rapidly into final states containing at least one γ (44%) or π^0 (55%), the latter decaying almost every time into 2γ . Because of the cut on the total energy sum of the pion and the photon most of this background is rejected, as the remaining particles also receive their part of the energy. Fig. 5.15 suggests to tighten this cut because the background would be much more affected than the real events. The count rates shown in this plot are obtained before making the q^2 cut.

Table 5.1 shows that the generated final state in all 34 cases contains a nucleon. This suggests that the nucleus was disintegrated in the reaction. The fragments are tracked by COMgeant, but there is no single particle ID to label them. Thus, they unfortunately are not part of the list of particles emerging from the primary vertex. Although every event contains particles with polar angles bigger than 20 deg it is not obvious that the target recoil detector mentioned in section 2.2.4 would see all of them as there is a certain probability for them to be stopped inside the target. Another simulation should be done to answer this question.

The statistics gathered after the cuts do not permit an analysis of the influence of the background on the measurement of the polarizabilities. The distribution of the background events in the $(\cos \theta, \omega)$ plane has to be closely examined as the determination of the polarizability parameters is very sensitive to local changes of the count rate. Since the real background rate for a Primakoff sample of 620.000 events would be about $2 \cdot 10^9$ it is impossible to study this directly. It could be done by step-wise loosening the q^2 cut to enable the extrapolation to the real background.

The overall signal to noise ratio for hadronic background can be estimated from the ratio of the cross sections and the background suppression. The hadronic interaction length of Lead of 194 g cm^{-2} corresponds to a cross section of 1.77 barn, the suppression factor of $26/4500000$ reduces this to $10 \text{ } \mu\text{barn}$. This has to be compared to the cross section of Primakoff Compton scattering—with a produced photon energy of at least 90 GeV—of about $500 \text{ } \mu\text{barn}$. The ratio of 50 neither does include the positive effect of the target recoil veto nor does it regard other background.

5 SIMULATION

	particle with P and θ		
1	π^-	75.464	0.1
	π^0	113.708	0.1
	π^0	3.965	2.7
	n	0.939	49.2
	π^+	0.496	21.3
	π^-	0.739	11.5
2	p^+	0.257	97.1
	π^-	31.900	0.2
	π^0	155.474	0.0
3	π^-	43.042	0.2
	π^0	144.547	0.1
	π^0	1.649	4.1
	n	0.679	39.7
	π^-	0.378	7.8
	π^+	0.474	27.8
4	η	100.321	0.1
	π^-	96.385	0.1
	η	0.506	26.2
	p^+	0.550	12.2
5	π^0	0.047	77.6
	η	96.178	0.1
	π^-	90.728	0.0
	p^+	1.305	18.8
	π^-	0.185	65.2
6	π^+	0.263	107.9
	π^0	0.329	25.5
	π^-	42.855	0.2
	π^0	146.881	0.0
7	p^+	0.109	41.2
	π^-	50.418	0.2
	π^0	136.763	0.0
8	p^+	0.367	42.1
	π^0	0.307	76.0
	n	0.179	33.3
9	π^-	38.250	0.2
	π^0	141.826	0.0
	π^-	55.075	0.1
10	π^0	136.945	0.1
	n	0.369	37.7
	π^0	0.208	94.0
	π^-	20.099	0.1
	π^0	160.664	0.0
	π^+	2.124	6.5
11	π^-	2.951	11.7
	η	2.294	22.1
	π^0	0.119	81.0
	p^+	1.101	14.5
	π^-	0.165	59.5
	p^+	0.140	75.7
12	π^-	47.200	0.2
	π^0	140.678	0.1
	p^+	0.269	59.5
	π^0	0.154	40.1
	π^-	36.390	0.2
13	π^0	150.498	0.0
	π^+	1.562	36.1
	n	0.957	37.4
	π^0	0.219	89.7
	n	0.243	120.8
14	π^-	23.391	0.2
	π^0	171.231	0.0
	π^-	40.821	0.3
15	π^0	147.336	0.0
	n	0.382	8.9
	π^0	0.231	127.5
	π^-	31.430	0.2
16	π^0	161.438	0.0
	n	0.538	33.0
	π^+	0.158	105.5
	π^-	51.488	0.2
	π^0	139.060	0.1
17	p^+	1.774	22.3
	π^0	0.507	24.4
	π^+	0.896	62.2
	π^-	0.440	24.4
18	π^-	34.750	0.2
	π^0	147.762	0.1
	n	0.220	80.4
	π^0	90.327	0.1
19	π^-	103.762	0.1
	π^-	2.018	24.6
	p^+	1.060	52.8
	π^0	0.157	76.4
	π^-	32.044	0.2
20	π^0	155.540	0.1
	π^+	2.146	8.0
	n	1.901	7.1
	π^+	0.252	75.0
	π^-	0.746	61.4
	π^-	0.890	46.7
21	π^-	81.077	0.1
	π^0	105.360	0.1
	p^+	0.983	32.7
	π^0	0.257	38.6
22	π^-	47.125	0.2
	π^0	142.599	0.1
	π^-	0.571	64.4
	p^+	0.616	52.1
23	π^-	47.125	0.2
	π^0	142.599	0.1
	π^-	0.571	64.4
	p^+	0.616	52.1
24	π^-	44.984	0.3
	π^0	144.410	0.1
	n	0.358	57.4
	π^0	0.316	49.2
25	π^-	23.114	0.3
	π^0	161.851	0.0
	π^-	1.036	22.2
	n	0.613	22.5
	π^0	0.552	17.4
	π^0	0.410	11.2
26	η	0.680	10.6
	π^+	1.478	16.4
	π^0	1.987	8.7
	η	127.480	0.0
27	π^-	56.346	0.2
	π^0	130.700	0.1
	π^+	3.777	7.6
	π^0	0.873	19.8
	n	1.060	10.4
28	π^-	0.278	55.0
	π^+	0.295	18.5
	π^0	0.791	44.0
	π^0	2.982	5.0
	π^0	0.464	67.1
	π^-	60.285	0.2
29	π^0	125.918	0.1
	π^-	1.088	32.3
	π^0	1.032	14.8
	p^+	1.634	8.8
30	π^0	0.739	9.6
	π^-	13.973	0.2
	π^0	174.799	0.0
	K^+	3.748	6.0
31	Λ	0.457	39.4
	π^-	71.699	0.1
	π^+	4.882	5.9
	η	4.221	2.9
	n	1.995	11.9
	p^+	0.254	10.9
	π^0	0.209	95.1
	π^-	42.076	0.3
	π^+	12.159	1.0
	π^0	23.350	0.4
	π^-	6.596	5.1
32	π^0	0.309	13.8
	π^-	2.750	1.4
	π^+	7.612	3.7
	π^0	1.319	7.8
33	π^-	0.349	35.2
	π^0	2.074	22.7
	π^+	1.220	12.6
	π^0	1.068	19.3
	π^0	0.315	56.3
34	π^-	92.685	0.2
	π^0	98.957	0.1
	n	0.647	15.3
	π^0	0.435	47.3
	π^0	0.451	113.6
35	π^-	77.530	0.2
	π^0	111.605	0.1
	n	2.658	7.9
	π^0	1.356	12.2
	π^-	17.554	0.2
36	π^0	166.683	0.0
	π^+	0.596	53.4
	n	0.796	14.4
	π^-	1.551	12.1
	π^0	0.124	92.3
37	K^+	4.558	3.0
	n	1.691	29.1
	π^-	37.495	0.2
	π^0	143.636	0.0
38	K_L	2.035	26.4
	π^-	18.527	0.1
39	π^0	162.495	0.0
	p^+	0.670	34.8
	π^-	0.418	26.4
	π^0	2.681	6.7
	π^-	0.442	34.3
40	π^+	0.815	33.5
	π^-	40.821	0.3
41	π^0	147.336	0.0
	n	0.382	8.9
	π^0	0.231	127.5
	π^-	31.430	0.2
42	π^0	161.438	0.0
	n	0.538	33.0
	π^+	0.158	105.5
	π^-	51.488	0.2
	π^0	139.060	0.1
43	p^+	1.774	22.3
	π^0	0.507	24.4
	π^+	0.896	62.2
	π^-	0.440	24.4
44	π^-	34.750	0.2
	π^0	147.762	0.1
	n	0.220	80.4
	π^0	90.327	0.1
45	π^-	103.762	0.1
	π^-	2.018	24.6
	p^+	1.060	52.8
	π^0	0.157	76.4
	π^-	32.044	0.2
46	π^0	155.540	0.1
	π^+	2.146	8.0
	n	1.901	7.1
	π^+	0.252	75.0
	π^-	0.746	61.4
	π^-	0.890	46.7
47	π^-	81.077	0.1
	π^0	105.360	0.1
	p^+	0.983	32.7
	π^0	0.257	38.6
48	π^-	47.125	0.2
	π^0	142.599	0.1
	π^-	0.571	64.4
	p^+	0.616	52.1
49	π^-	47.125	0.2
	π^0	142.599	0.1
	π^-	0.571	64.4
	p^+	0.616	52.1
50	π^-	44.984	0.3
	π^0	144.410	0.1
	n	0.358	57.4
	π^0	0.316	49.2
51	π^-	23.114	0.3
	π^0	161.851	0.0
	π^-	1.036	22.2
	n	0.613	22.5
	π^0	0.552	17.4
	π^0	0.410	11.2
52	η	0.680	10.6
	π^+	1.478	16.4
	π^0	1.987	8.7
	η	127.480	0.0
53	π^-	56.253	0.1
	p^+	0.157	45.8
	π^-	18.527	0.1
	π^0	162.495	0.0
	p^+	0.670	34.8
54	π^-	0.418	26.4
	π^0	2.681	6.7
	π^-	0.442	34.3
	π^+	0.815	33.5
	π^-	40.821	0.3
55	π^0	147.336	0.0
	n	0.382	8.9
	π^0	0.231	127.5
	π^-	31.430	0.2
56	π^0	161.438	0.0
	n	0.538	33.0
	π^+	0.158	105.5
	π^-	51.488	0.2
	π^0	139.060	0.1
57	p^+	1.774	22.3
	π^0	0.507	24.4
	π^+	0.896	62.2
	π^-	0.440	24.4
58	π^-	34.750	0.2
	π^0	147.762	0.1
	n	0.220	80.4
	π^0	90.327	0.1
59	π^-	103.762	0.1
	π^-	2.018	24.6
	p^+	1.060	52.8
	π^0	0.157	76.4
	π^-	32.044	0.2
60	π^0	155.540	0.1
	π^+	2.146	8.0
	n	1.901	7.1
	π^+	0.252	75.0
	π^-	0.746	61.4
	π^-	0.890	46.7
61	π^-	81.077	0.1
	π^0	105.360	0.1
	p^+	0.983	32.7
	π^0	0.257	38.6
62	π^-	47.125	0.2
	π^0	142.599	0.1
	π^-	0.571	64.4
	p^+	0.616	52.1
63	π^-	47.125	0.2
	π^0	142.599	0.1
	π^-	0.571	64.4
	p^+	0.616	52.1
64	π^-	44.984	0.3
	$\pi^$		

5.6 Influence of systematic reconstruction errors

As the tracking stations in the spectrometer will not be perfectly aligned there will be systematic reconstruction errors. While a shifted direction can be easily detected and corrected by looking at the transverse momentum transfer components (fig. 5.7 and 5.8), energy reconstruction errors are a serious source of uncertainty. If both—pion and photon—have the same relative reconstruction error these will approximately cancel during the Lorentz transformation to the projectile frame, but if the errors are different the event will be shifted in the $(\cos \theta, \omega)$ plane. This effect is seen even in the perfectly aligned Monte Carlo spectrometer because of the longitudinal energy leakage of the ECAL, resulting in less energy of the photon. To compensate this effect the reconstructed energy was multiplied by a factor of 1.02 so that the mean reconstructed energy matches the generated one. Methods to detect and compensate such systematic errors should be further investigated.

Chapter 6

Conclusion and Outlook

The single particle detection properties of the COMPASS spectrometer have been evaluated by means of several simulations. The key data are a momentum resolution for pions of 1% above 35 GeV and up to 2.5% below 35 GeV accompanied by an angular resolution of 7.9 mrad GeV/ p and an energy resolution for photons of 1.5% above 90 GeV accompanied by an angular resolution of 30 μ rad. It is proposed to investigate the use of a pre-shower for the second electromagnetic calorimeter to reduce the longitudinal energy leakage out of this detector that worsens the resolution of the photon energy. The photon reconstruction inefficiency is given by the conversion probability before leaving the second spectrometer magnet; the corresponding efficiency is 58%. The single pion reconstruction efficiency is about 92%.

With the validated setup a simulation of Primakoff Compton scattering of π^- on Lead at a beam energy of 190 GeV has been done for five different pairs of polarizability parameters with a statistics of five times 620.000 events, each sample corresponding to half a day of COMPASS data taking. A method to reconstruct the beam energy in the case when only the beam particle's direction is known has been developed. The reconstruction efficiency for Primakoff events has been measured and amounts to 50–55%, slightly depending on the photon energy. It has been shown that the Coulomb peak—caused by the q^{-4} behavior of the cross section—is retained in the reconstruction and permits a cut of $q^2 > -1000 \text{ MeV}^2$. The effect of this cut on the hadronic background generated with Fritiof has been studied, coming to the conclusion that even without a target recoil veto detector a signal to noise ratio of 50 is achievable. However further improvement is necessary as the extraction of the polarizabilities is very sensitive to distortions of the differential cross section. This has been tested with the five Primakoff samples. It has been shown that one month of COMPASS data taking would result in statistical errors of $0.02 \cdot 10^{-4} \text{ fm}^3$ for $\bar{\alpha} + \bar{\beta}$ and $0.14 \cdot 10^{-4} \text{ fm}^3$ for $\bar{\alpha} - \bar{\beta}$, thus it is

6 CONCLUSION AND OUTLOOK

desirable to perform this measurement at COMPASS.

It also became clear that further investigation is necessary to make full use of the big statistics. Systematic shifts have been observed, both in the reconstructed polarizabilities and in those obtained by fitting the cross section to the output of the generator. The reason for this discrepancy remains to be found. It has been proposed to more closely study the influence of the background on the retrieval of the polarizability parameters. Further optimization of the kinematic reconstruction—specifically including the measurement of the beam momentum—is possible.

Appendix A

Design of the computing cluster

To reach the high statistics that was necessary in the context of this thesis a parallel ansatz was used. Since the single events are independent of each other the software chain as described in chapter 4 was run on 32 machines in parallel, two jobs on each node.

A.1 The hardware

Each machine was equipped with two Celeron 400 CPUs, 256MB memory and 84GB hard disk space, making a total of 8GB memory and 2688GB hard disk space. The cluster was controlled by a server featuring two Pentium III CPUs with 450 MHz, 512MB memory and 250GB hard disk space. The computing nodes were connected via a 100baseTX switched network with a 1000baseSX uplink to the server.

Since the maximum disk throughput of the server was limited to 20MB/ sec the rather huge ZEBRA files of the intermediate step were kept locally on the computing nodes. Due to a file size limitation of 2GB the number of events per run was limited. While a single particle event with interactions disabled occupies about 10kB a full Fritiof event easily exceeds 250kB. Thus a maximum of 7000–200000 events per job could be processed, depending on the settings.

A.2 The software

To have most flexibility in the programming of the Monte Carlo production cycle, Linux was used as operating system. Since tracking and reconstruction only

require the execution of one program each this procedure was controlled by shell scripts utilizing rsh. On each cluster node two directories were setup to allow the parallel execution of two jobs. These were started after the setting of some environment variables by a local script which in turn was triggered by a script utilizing rsh on the server.

A.3 Performance

type	events	generator [sec]	COMgeant [sec]	CORAL [sec]	per event [sec]
A	10000	1.3 ± 0.5	483 ± 16	5210 ± 50	0.57 ± 0.01
B	10000	1.3 ± 0.5	33800 ± 565	7084 ± 65	4.09 ± 0.06
	20000	1.3 ± 0.5	67728 ± 786	14133 ± 151	4.09 ± 0.04
C	10000	1.3 ± 0.5	81149 ± 1390	3661 ± 54	8.48 ± 0.14
D	10000	0 ± 0	90290 ± 915	27367 ± 256	11.77 ± 0.10
E	5000	5021 ± 55	61481 ± 762	4107 ± 61	14.12 ± 0.16
F	5000	0 ± 0	69198 ± 796	17202 ± 2142	17.28 ± 0.45
G	10000	9713 ± 82	172693 ± 2437	13986 ± 1625	19.64 ± 0.27

Table A.1: Computing times on the cluster

Table A.1 shows the computing times for various job sizes on a single node for different event types. As Fritiof is built into COMgeant no timing could be measured for its execution time.

type A: single π^- events with all interactions disabled

type B: single π^- events with all interactions enabled

type C: single γ events with all interactions enabled

type D: Fritiof minimum bias events without pileup

type E: Polaris Primakoff events without pileup

type F: Fritiof minimum bias events with pileup

type G: Polaris Primakoff events with pileup

Appendix B

Single particle generator

```
//
// This is a generator for single particle events
//
// momentum is randomized in a momentum cone defined by
// angle (theta range) and total momentum range (p)
//
// cos(theta) is randomized to get homogenous solid angle
// distribution - flat theta distribution is also possible
//
// the output goes as formatted input fort.26 to COMgeant
//
// usage: charged [options]
// -e <number of events to simulate [160]>
// -s <random seed 0<n<9000000000 >
// -a <min theta [0]>
// -A <max theta [5mrad]>
// -f flat theta distribution
// -p <min momentum in GeV [0.5]>
// -P <max momentum in GeV [200]>
// -t <particle type [9]>
//

#include <iostream.h>
#include <iomanip.h>
#include <fstream.h>
#include <stdlib.h>
#include <unistd.h>
#include <math.h>

//I am using the cernlib random numbers (fortran code)
```

B SINGLE PARTICLE GENERATOR

```
extern "C" {
    void rmarut_(int&,int&,int&);
    void rmarin_(int&,int&,int&);
    void ranmar_(float*,int&);
}

void events(int n,float minangle,float maxangle,int flat,
            float pmin,float pmax,int type)
{
    float rnum[3],px,py,pz,phi,theta,p;
    double mintrange,maxtrange,trange;
    int num=3;
    ofstream out("generated.dat");

    mintrange=cos(minangle);
    maxtrange=cos(maxangle);
    trange=mintrange-maxtrange;

    for(int i=0;i<n;i++) {
        ranmar_(rnum,num);
        // randomize momentum and angle
        p=rnum[0]*(pmax-pmin)+pmin; //momentum pmin<p<pmax GeV
        phi=rnum[1]*6.2831853072; //phi is symmetrical
        if(!flat) {
            theta=acos(maxtrange+rnum[2]*trange); //correct area element
        } else {
            theta=minangle+rnum[2]*(maxangle-minangle);
        }

        // transform to cartesian coordinates
        pz=p*sinf(theta)*cosf(phi);
        py=-p*sinf(theta)*sinf(phi);
        px=p*cosf(theta); // particle going into x-direction

        // make formatted output for COMgeant
        out<<" 1"<<endl;
        out.form(" % 9.3f % 9.3f % 9.3f\n",0.,0.,0.);
        out.form("% 6d % 9.4f % 9.4f % 9.4f\n",type,px,py,pz);
    }
}
```

```

int main(int argc, char**argv)
{
    int IJKL, NTOT1, NTOT2;
    int c, seed=0, num_events=160, flat=0, type=9;
    float minangle=0, maxangle=0.005, pmin=0.5, pmax=200.;

    // check command line arguments (see above)
    while((c=getopt(argc, argv, "s:e:a:A:p:P:t:f"))!=-1) {
        switch(c) {
            case 's':
                seed=strtol(optarg, NULL, 0);
                break;
            case 'e':
                num_events=strtol(optarg, NULL, 0);
                break;
            case 'a':
                minangle=strtod(optarg, NULL);
                break;
            case 'A':
                maxangle=strtod(optarg, NULL);
                break;
            case 'p':
                pmin=strtod(optarg, NULL);
                break;
            case 'P':
                pmax=strtod(optarg, NULL);
                break;
            case 'f':
                flat=1;
                break;
            case 't':
                type=strtol(optarg, NULL, 0);
                break;
        }
    }

    // seed random number generator if requested
    if(seed) {
        rmarut_(IJKL, NTOT1, NTOT2);
        rmarin_(seed, NTOT1, NTOT2);
    }
}

```

B SINGLE PARTICLE GENERATOR

```
// do the work
cout<<num_events<<" "<<minangle<<" "<<maxangle<<" "
    <<pmin<<" "<<pmax<<" "<<quiet<<" "<<type<<endl;
events(num_events,minangle,maxangle,flat,pmin,pmax,quiet,type);

// nothing will fail ;- )
return 0;
}
```

Appendix C

The detector setup

In front of the target two scintillating fiber stations and two silicon stations form a beam telescope. The angle of scattered particles is then measured between the target and SM1 by two silicon stations, two Micromegas and two scintillating fiber stations.

After SM1 three GEMs each accompanied by a silicon station perform the small angle tracking before the RICH while low energy or high p_T particles are tracked by a drift chamber and a stack of straw chambers. Mounted on the RICH entrance window is a scintillating fiber station.

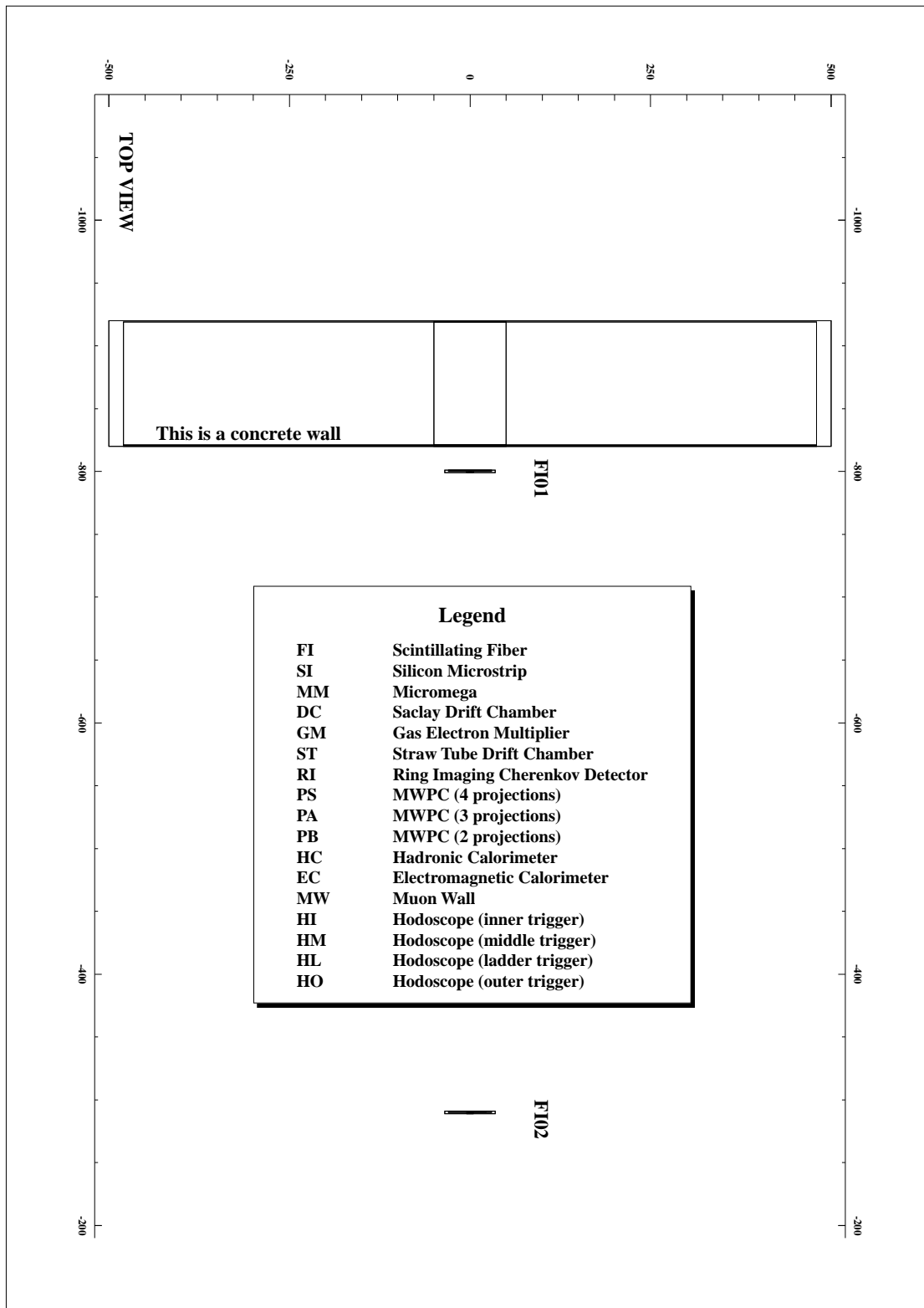
After the RICH two types of tracking stations are used: an MWPC and a GEM are accompanied either by a silicon station (type A) or a scintillating fiber station (type B). Directly downstream of the RICH resides a station of type A. The empty space between this station and HCAL1 will be used up by ECAL1. Upstream and downstream of the first muon wall a station of type B and A respectively are mounted.

Directly after SM2 three MWPCs with one GEM each are stacked with one silicon and one scintillating fiber station. The large space between these trackers and the type B station just in front of the hodoscope and the second set of calorimeters will be used in the future by the second RICH.

Downstream of HCAL2 behind the second muon wall are hodoscopes and MWPCs for muon identification and the muon trigger. These are not detailed since they were not of primary interest for Primakoff events.

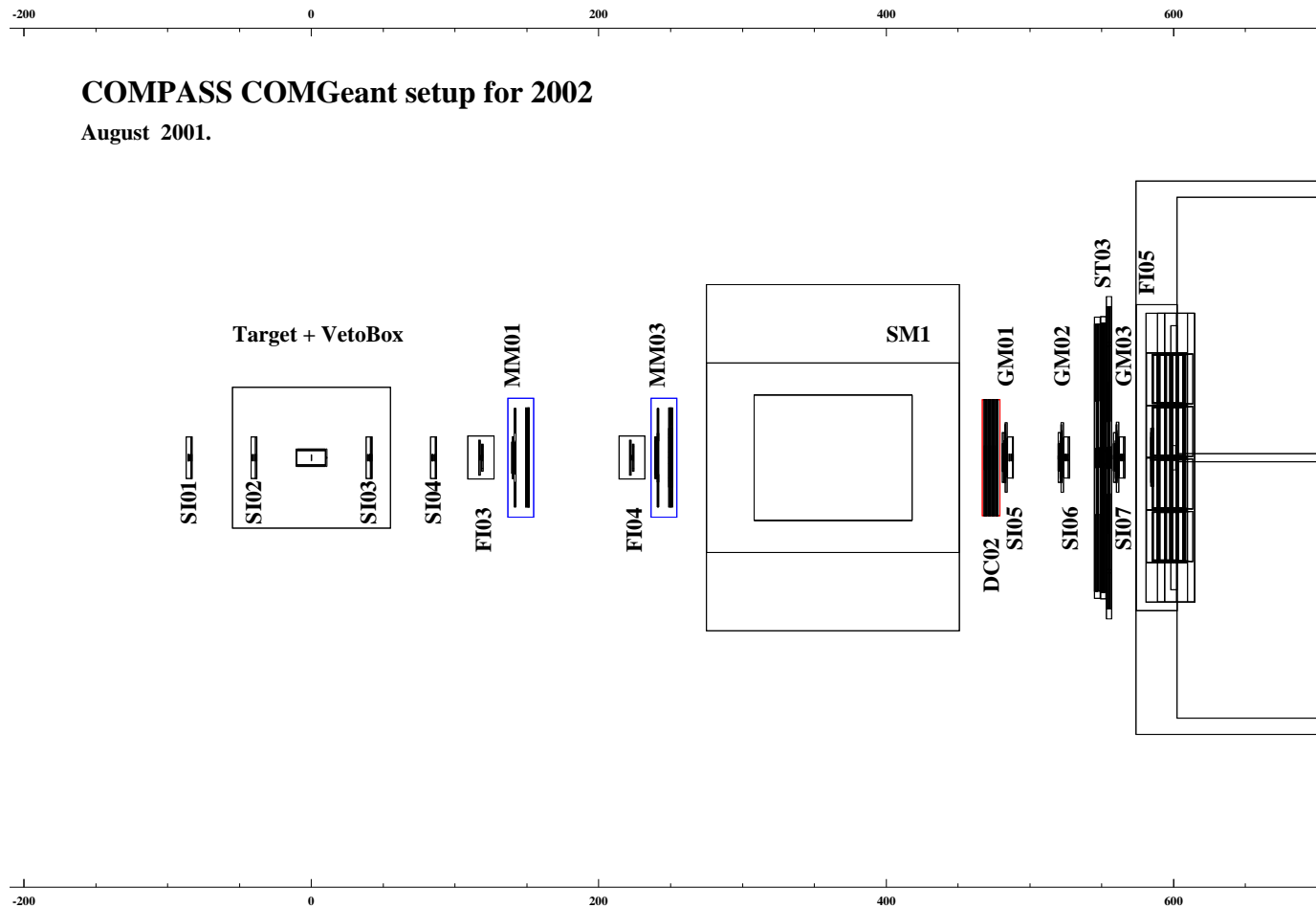
The drawings on the following pages depict the detector setup by showing the COMgeant volumes that constitute each detector station. The script to produce the drawings was provided by [Ger01].

C THE DETECTOR SETUP

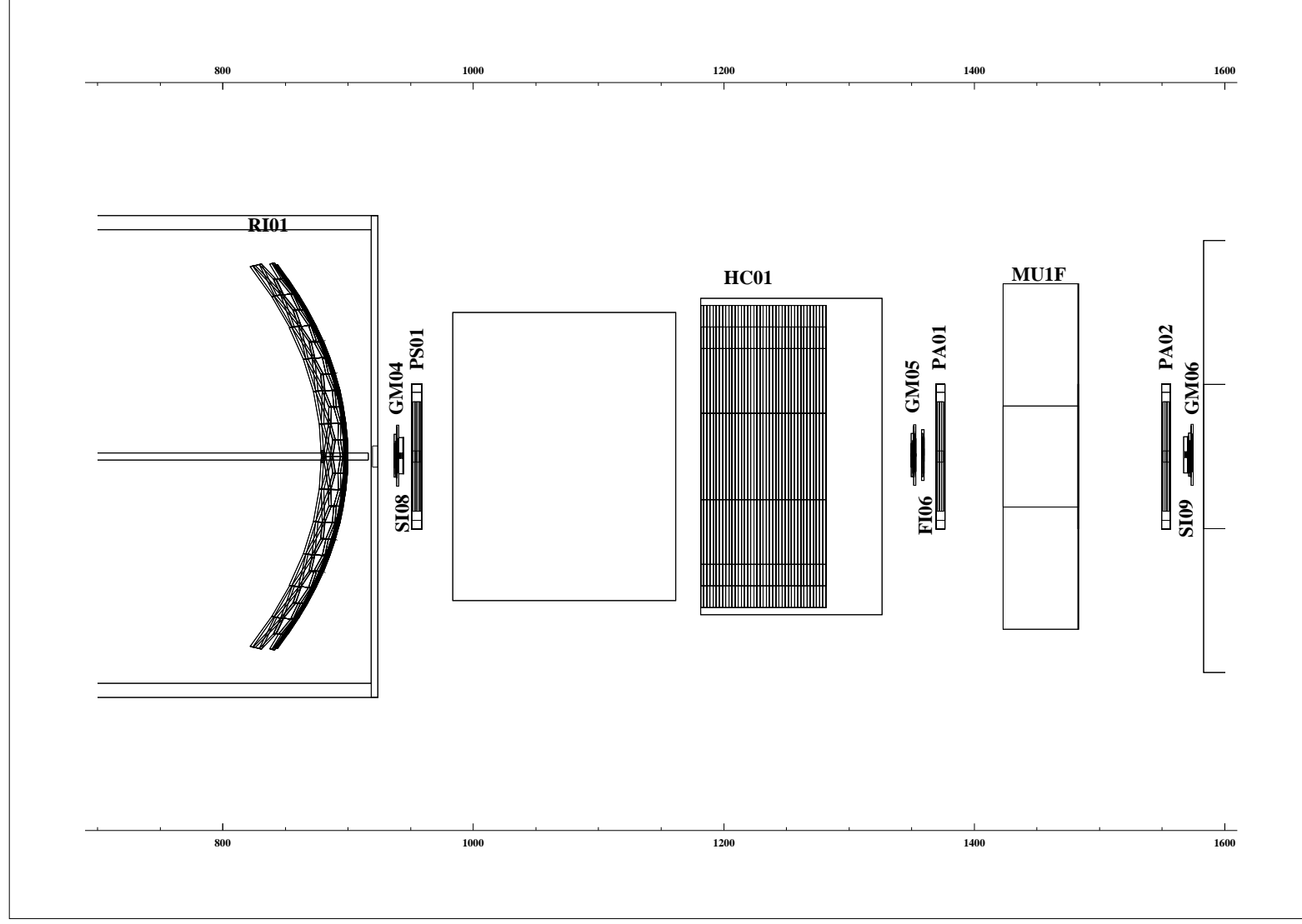


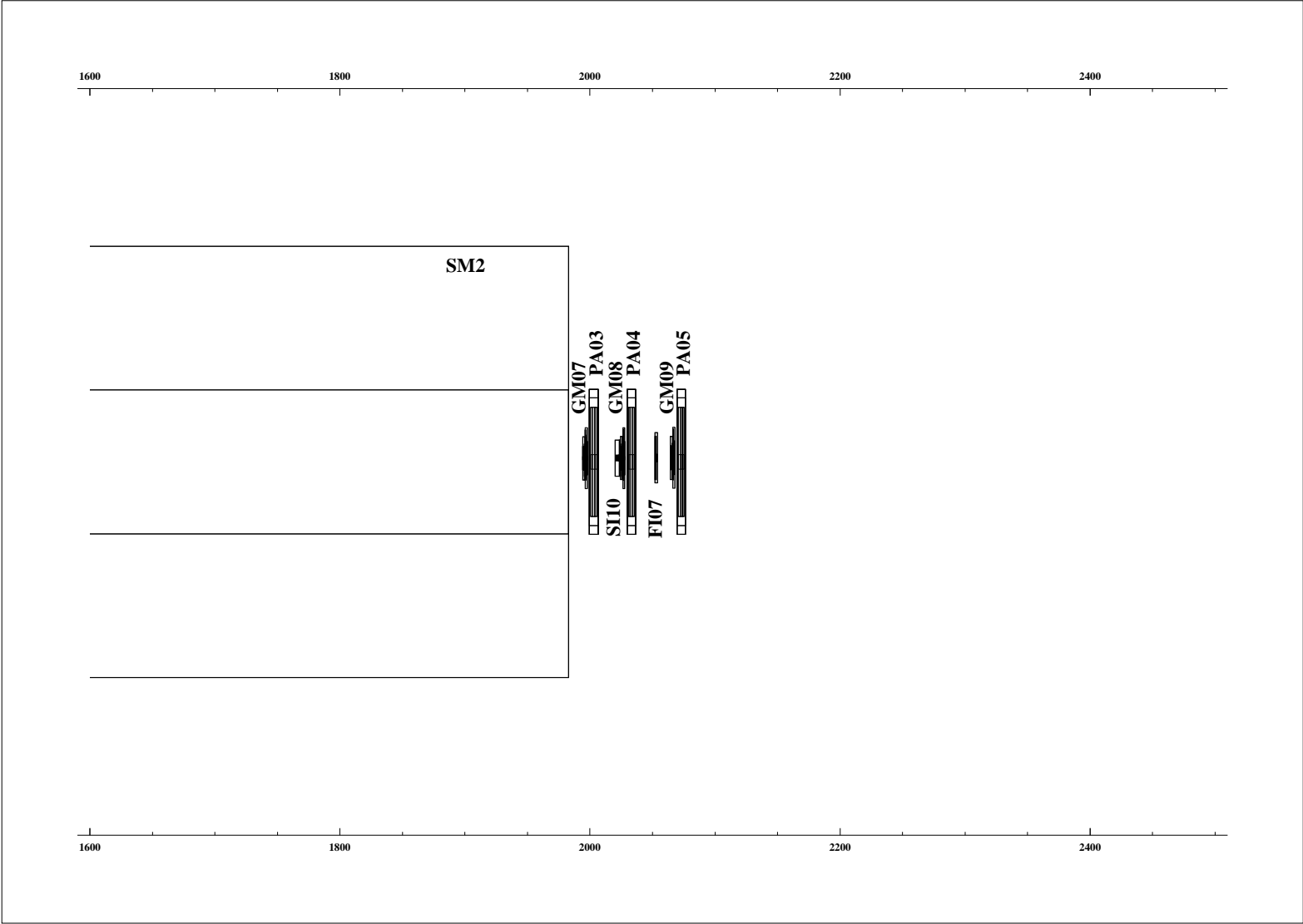
COMPASS COMGeant setup for 2002

August 2001.

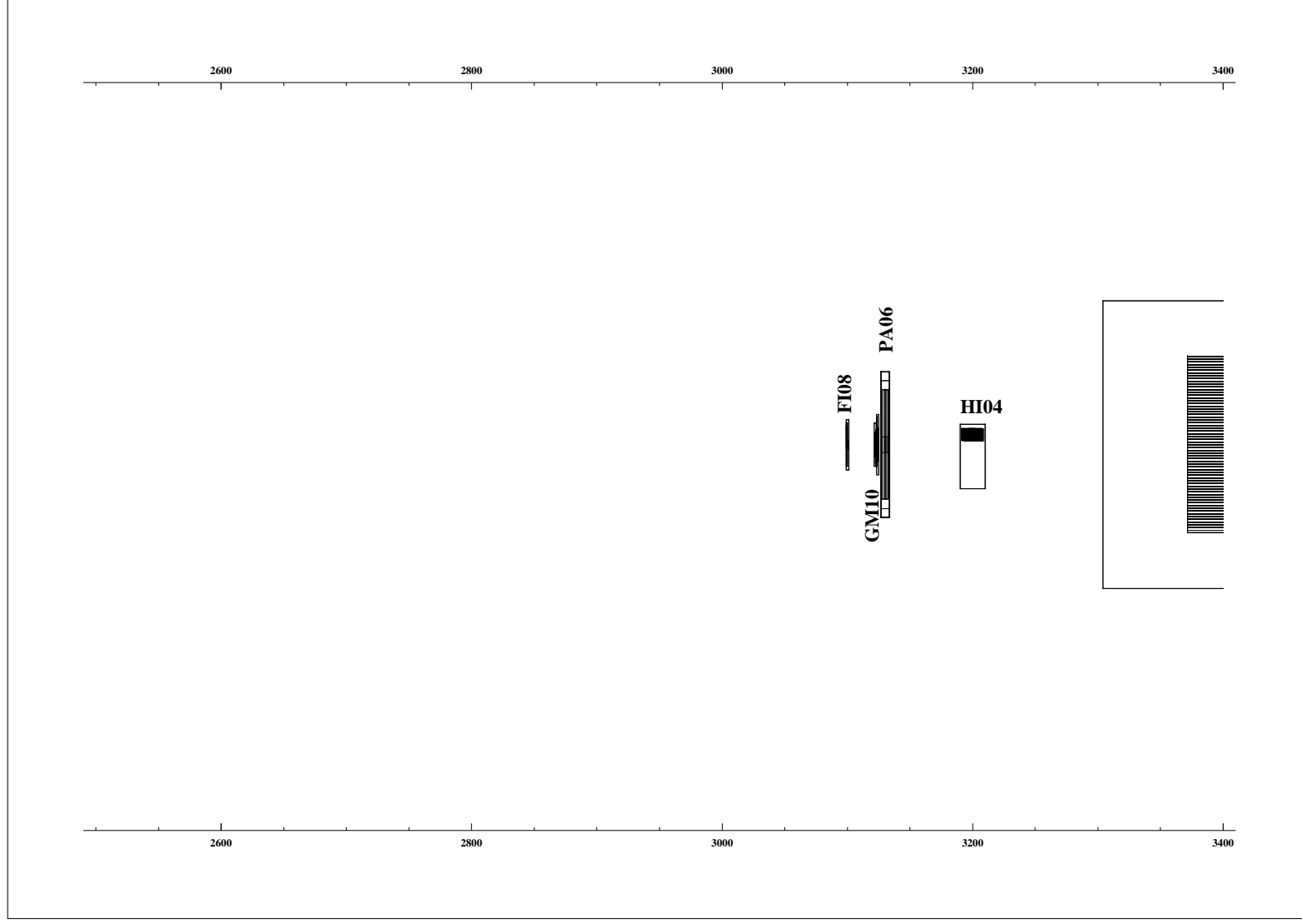


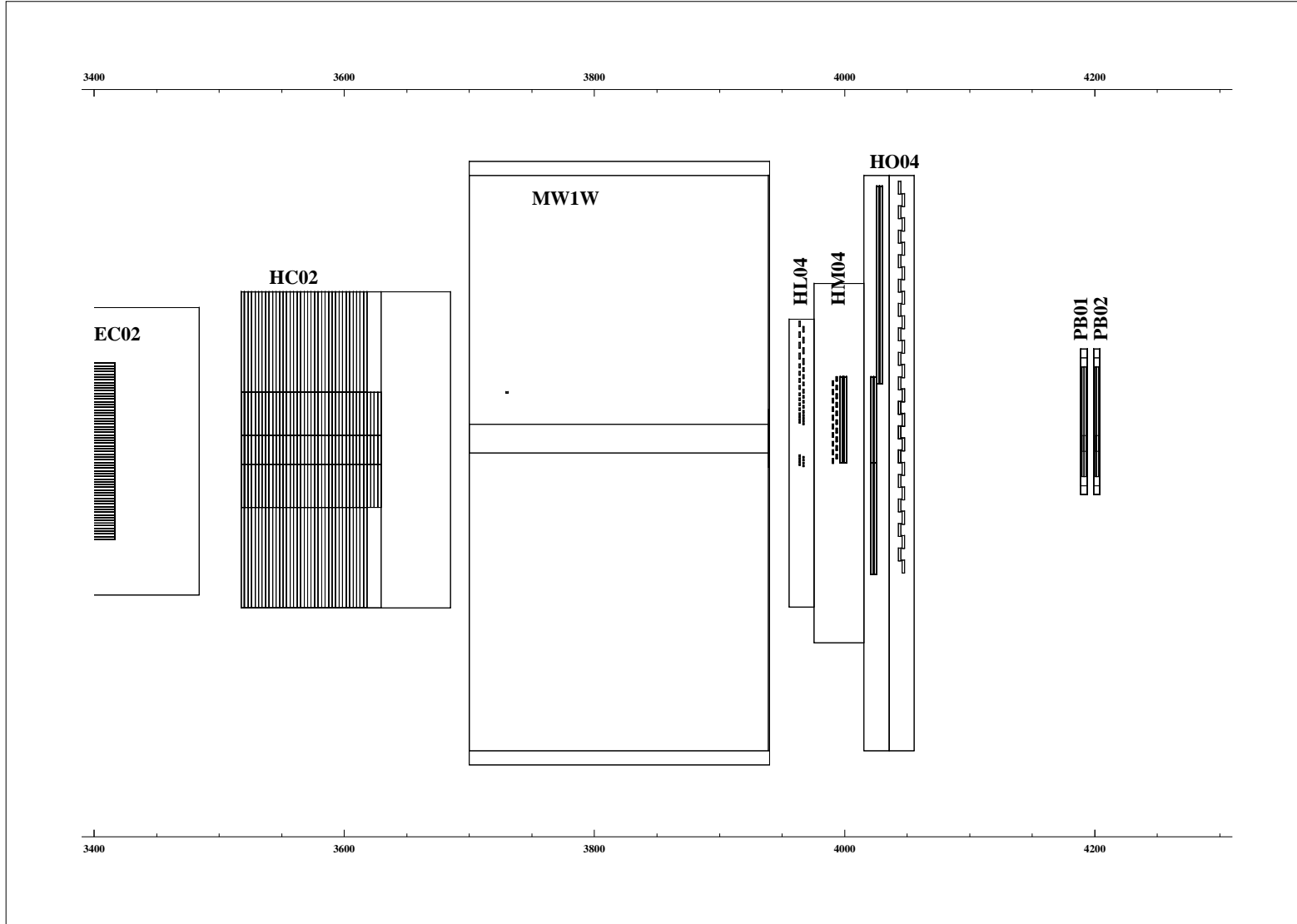
C THE DETECTOR SETUP



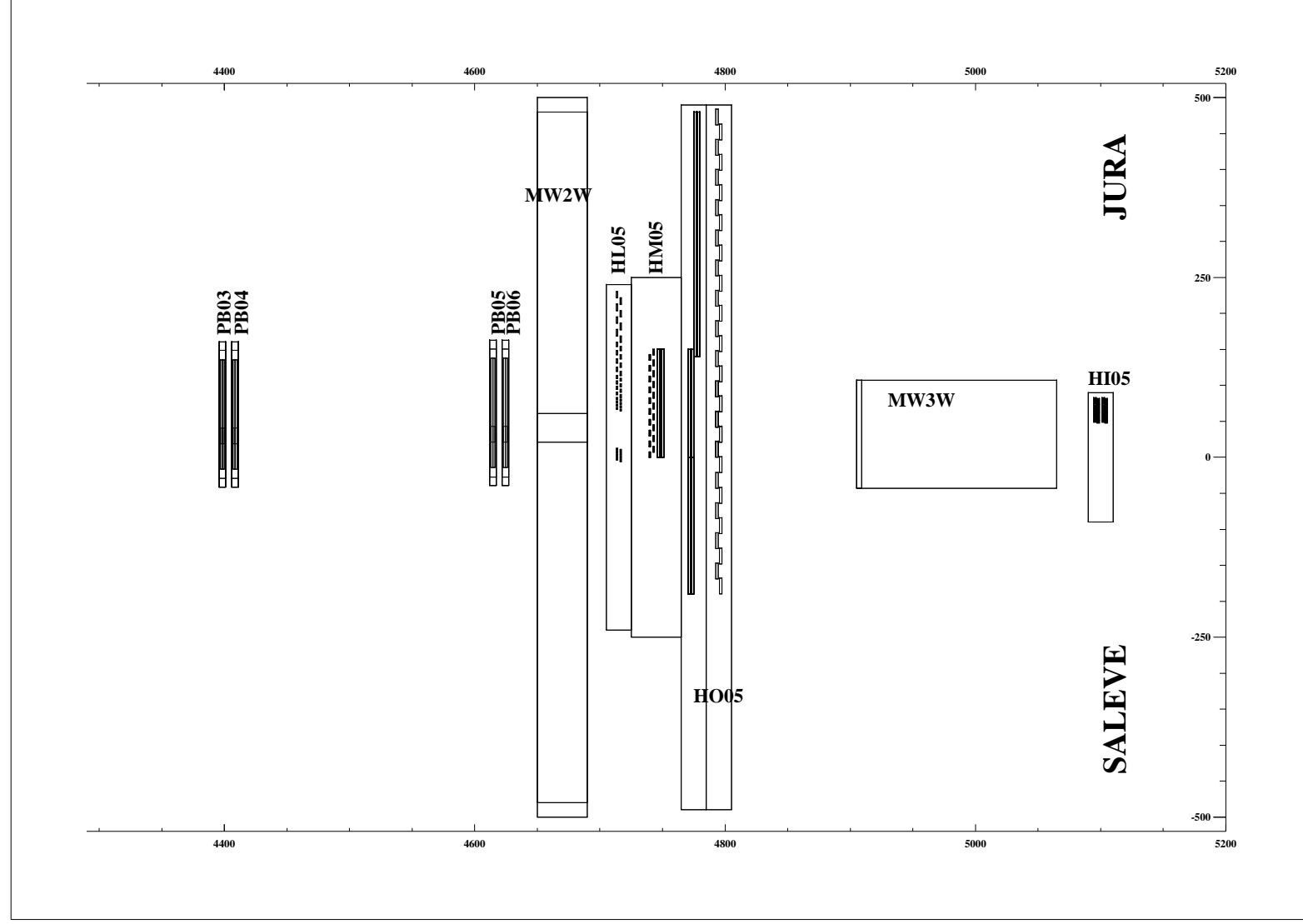


C THE DETECTOR SETUP





C THE DETECTOR SETUP



Bibliography

- [A⁺85] Y. M. Antipov et al. Experimental estimation of the sum of pion electrical and magnetic polarizabilities. *Z. Phys. C* **26**, 495–497 (1985).
- [B⁺85] F. Binon et al. The GAMS-4000 electronic calorimeter. *CERN Preprint SPSC 84-45*, 214 (1985).
- [B⁺90] J. Bijnens et al. Three pseudoscalar photon interactions in chiral perturbation theory. *Phys. Lett. B* **237**, 488 (1990).
- [B⁺94] S. Belucci et al. Low energy photon-photon collisions to two-loop order. *Nucl. Phys. B* **423**, 80–122 (1994).
- [Bal60] A. M. Baldin. Polarizability of nucleons. *Nucl. Phys.* **18**, 310 (1960).
- [Bué95] M. Buénerd. Prospects for hadron electromagnetic polarizability measurement by radiative scattering on a nuclear target. *Nucl. Instr. and Meth. in Phys. Res. A* **361**, 111–128 (1995).
- [Bür96] U. Bürgi. Pion polarizabilities and charged pion-pair production to two loops. *Nucl. Phys. B* **479**, 392–426 (1996).
- [CE92] The CELLO collaboration. An experimental study of the process $\gamma\gamma \rightarrow \pi^+\pi^-$. *Z. Phys. C* **56**, 381–390 (1992).
- [CHE95] Yu. Alexandrov et al. CHEOPS. *CERN SPSLC 95-22* March 1995. Letter of intent.
- [CO96] COMPASS collaboration. Common Muon and Proton Apparatus for Structure and Spectroscopy. *CERN SPSLC 96-14* (1996).
- [Col93] J. Collins. Fragmentation of transversely polarized quarks probed in transverse momentum distributions. *Nucl. Phys. B* **396**, 161–182 (1993).
- [CPv] Steffen Görzig, steffen.goerzig@informatik.uni-stuttgart.de. CPPvm home page, <http://www.informatik.uni-stuttgart.de/ipvr/bv/cppvm/>.

BIBLIOGRAPHY

- [EMC88] The European Muon Collaboration. A measurement of the spin asymmetry and determination of the structure function $g(1)$ in deep inelastic muon - proton scattering. *Phys. Lett.* **B 206**, 364 (1988).
- [EMC89] The European Muon Collaboration. An investigation of the spin structure of the proton in deep inelastic scattering of polarized muons on polarized protons. *Nucl. Phys.* **B 328**, 1 (1989).
- [FG72] H. Fritzsch and U. Gell-Mann. XVI Int. Conf. on High Energy Physics, page 135, Chicago, 1972.
- [Fli97] Torsten Fließbach. *Elektrodynamik*. Spektrum Akad. Verl., 1997. German book on electrodynamics.
- [Fri] Hong Pi, pihong@thep.lu.se. Fritiof documentation (postscript), <http://wwwinfo.cern.ch/asdoc/psdir/fritiof.ps.gz>.
- [Fri01] Jan M. Friedrich, friedrich@e18.physik.tu-muenchen.de. Private communication, August 2001.
- [Gea] Vadim Alexakhine et al., Vadim.Alexakhine@cern.ch. COMgeant page, <http://valexakh.home.cern.ch/valexakh/wwwcomg/index.html>.
- [Ger01] Sergei Gerassimov, ges@mail.cern.ch. Private communication, August 2001.
- [GR88] M. Glück and E. Reya. Spin dependent parton distributions in polarized deep inelastic lepton nucleon scattering. *Z. Phys.* **C 39**, 569 (1988).
- [GSR87] C. Gignoux, B. Silvestre-Brac, and J. M. Richard. Possibility of stable multi - quark baryons. *Phys. Lett.* **B 193**, 323 (1987).
- [Hei54] W. Heitler. *The Quantum Theory of Radiation*. Monographs on Physics. Oxford University Press, third edition, 1954.
- [HMC95] E. Nappi et al. Semi-inclusive muon scattering from a polarised target. *CERN SPSLC 92-27* March 1995. Letter of intent.
- [JJ91] R.L. Jaffe and Xiang-Dong Ji. Chiral odd parton distributions and drell-yan processes. *Phys. Rev. Lett.* **67**, 552–555 (1991).
- [JJ92] R.L. Jaffe and Xiang-Dong Ji. Chiral odd parton distributions and drell-yan processes. *Nucl. Phys.* **B 375**, 527–560 (1992).
- [KS92] A. E. Kaloshin and V. V. Serebryakov. Crystal Ball experiment on $\gamma\gamma \rightarrow \pi^0\pi^0$ and neutral pion polarizability. *Phys. Lett.* **B 278**, 198–201 (1992).

- [Low54] F. E. Low. Scattering of light of very low frequency by systems of spin $1/2$. *Phys. Rev.* **96**, 1428 (1954).
- [Ma90] Mark II collaboration. Two-photon production of pion pairs. *Phys. Rev. D* **42**, 1350–1367 (1990).
- [MIN] F. James. MINUIT documentation, <http://wwwinfo.cern.ch/asdoc/minuit/minmain.html>.
- [MK84] T. Mayer-Kuckuk. *Kernphysik*. Teubner, 1984. German book on nuclear physics.
- [Olc01] Alexander Olchevski, Alexander.Olchevski@cern.ch. Private communication, October 2001.
- [PDG00] D. E. Groom et al. Review of particle physics. *Eur. Phys. J. C* **15**, 1–878 (2000).
- [Pei92] A. Peisert. Silicon microstrip detectors. *DELPHI 92-143 MVX 2* (1992).
- [Pet64] V. A. Petrunkin. Scattering of low-energy photons on a zero-spin particle. *Nucl. Phys.* **55**, 197–206 (1964).
- [Pet81] V. A. Petrunkin. Electric and magnetic polarizability of hadrons. *Sov. J. Part. Nucl.* **12(3)**, 278–302 (1981).
- [Pri51] H. Primakoff. Photo-production of neutral mesons in nuclear electric fields and the mean life of the neutral meson. *Phys. Rev.* **81**, 899 (1951).
- [PS61] Y. Pomeranchuk and M. Shmushkevich. On processes in the interaction of γ -quanta with unstable particles. *Nucl. Phys.* **23**, 452–467 (1961).
- [PVM] Jack Dongarra, dongarra@cs.utk.edu. PVM home page, http://www.epm.ornl.gov/pvm/pvm_home.html.
- [Ric91] Jean Marc Richard. Tetraquarks, pentaquarks and hexaquarks. *Nucl. Phys. Proc. Suppl.* **B 21**, 254–257 (1991).
- [ROO] René Brun and Fons Rademakers, Rene.Brun@cern.ch. ROOT web page, <http://root.cern.ch>.
- [Sau77] F. Sauli. Principles of operation of multiwire proportional and drift chambers. *CERN 77-09* (1977).
- [Sau97] F. Sauli. GEM: a new concept for electron amplification in gas detectors. *Nucl. Instr. and Meth. in Phys. Res. A* **386**, 531 (1997).

BIBLIOGRAPHY

- [SDC] Hugo Pereira, pereira@hep.saclay.cea.fr. Saclay drift chambers, <http://h.home.cern.ch/h/hpereira/www/index.html>.
- [Sim01] Frank Simon. *Commissioning of the GEM Detectors in the COMPASS Experiment*. Diploma thesis, TU München, November 2001.
- [Str97] B. Stroustrup. *The C++ Programming Language*. Addison-Wesley, third edition, June 1997.
- [SW99] M. Sans and U. Wiedner. Test beam results of 2 prototype straw tube chambers for COMPASS. *COMPASS-Note 2* (1999). <http://wwwcompass.cern.ch/compass/notes/1999-2/1999-2.ps.gz>.
- [T⁺01] D. Thers et al. Micromegas as a large microstrip detector for the COMPASS experiment. *Nucl. Instr. and Meth. A* **469**, 113–146 (2001).
- [Teu01] Andreas Teufel, Andreas.Teufel@cern.ch. Private communication, September 2001.
- [Z⁺86] M. Zielinski et al. Experimental constraints on $J^{PC} = 1^{-+}, I = 1$ hybrid mesons. *Z. Phys. C* **31**, 545 (1986).
- [ZEB] Jamie Shiers, shiers@cern.ch. Zebra documentation, http://wwwinfo.cern.ch/asdoc/zebra_html3/zebramain.html.

Own contributions

This thesis was done in the context of the COMPASS collaboration while the infrastructure was provided by the chair of Prof. Paul at the Technische Universität München. The existing computer cluster was outfitted with software from CERN with the help of Lars Schmitt. This includes the CERNLIB, COMgeant, CORAL and ROOT. The present author has created the environment to run the software in parallel and to collect the results. In the detector description several bugs were eliminated, it was adapted to the projected setup for the 2002 run and tested with events from a self-written generator. The acceptance and efficiency for single pion and photon events have been studied. A simulation of Primakoff scattering has been done and a large sample of hadronic background has been generated. Selection criteria for Primakoff events have been established and tested and the influence of the apparatus on the measured differential Primakoff Compton cross section has been evaluated. The amount of accepted hadronic background and the expected number of Primakoff Compton scattering events have been estimated.

Acknowledgements

First I would like to thank Prof. Stephan Paul for letting me study such an interesting topic and giving guidance on the approach to the problem.

Then I would like to thank Jan Friedrich for many fruitful discussions both about general physics questions and specific issues connected to this work. Also he was of great help debugging this thesis.

The same is true about Lars Schmitt, with his great knowledge of computer networks, CERN software and many other things. Also he had the right word in the right moment to make me work harder and finally achieve my goal.

Next there are many people whom I bothered with numerous questions and who helped me to understand the function and interplay of the various subsystems of the COMPASS spectrometer. Here I appreciated much the discussions with Boris Grube, Igor Konorov, Robert Wagner and Michael Wiesmann.

While taking care of the setup I received prompt and precise answers to my questions from Vadim Alexakhine, Alexander Zviaguine, Sergei Gerassimov, Alexander Olchevski and others. Thank you all for your great help.

Der größte Dank gilt meinen Eltern, die mich immer unterstützt und gefördert haben, selbst als ich mich entschied, nicht Musik zu studieren. Ebenso danken möchte ich meiner Freundin Alex, daß sie meine Physikbesessenheit tapfer erträgt und mich aufheitert, wenn mal wieder ein Programm nicht funktioniert hat. Außerdem hat sie dafür gesorgt, daß ich nicht vergesse, daß es ein Leben nach der Diplomarbeit gibt.